Catalytic conversion of glycerol to bio-based aromatics

He, Songbo

DOI:
10.33612/diss.222277430

Chapter 2

Catalytic conversion of pure glycerol over an un-modified H-ZSM-5 zeolite to bio-based aromatics

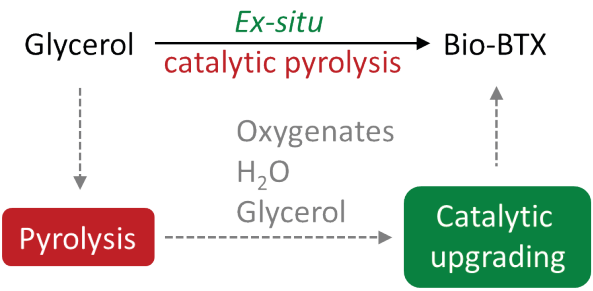

This chapter is adapted from:

Songbo He, Kenny Zuur, Dian Sukmayanda Santosa, André Heeres, Chuncheng Liu, Evgeny Pidko, Hero Jan Heeres, ***Applied Catalysis B-Environmental****, 2021, 281: 119467.*

Abstract

The catalytic conversion of pure glycerol to bio-aromatics (bio-BTX) over an un-modified H-ZSM-5 (SiO_2/Al_2O_3 molar ratio of 23) *via* an *ex-situ* catalytic pyrolysis approach in a continuous tandem-micro reactor at a scale of 1 g glycerol h^{-1} was investigated. A BTX peak carbon yield of 28.1 ± 0.2% was obtained at a pyrolysis temperature of 400 °C, catalytic upgrading temperature of 500 °C, atmospheric pressure and a WHSV of 1 h^{-1}. About 70% of the bound oxygen in glycerol was converted to water. The latter was mainly formed in the catalytic upgrading unit (70%), though conversion of glycerol to other oxygenates with water formation was also observed in the pyrolysis unit. Catalyst deactivation occurs at a time scale of hours and is mainly due to coke deposition (12.0 wt.%) on the catalyst surface. An oxidative regeneration procedure to remove coke was applied and 5 cycles of reaction-regeneration were performed successfully, though a drop in activity was observed after each cycle due to irreversible catalyst deactivation. Characterization of the fresh, deactivated and regenerated catalysts by various techniques revealed dealumination of the H-ZSM-5 framework and resulted in a dramatic decrease in Brønsted acidity of the catalyst. Dealumination mainly occurred in the catalytic upgrading reactor and to a by far lesser extent during catalyst regeneration. This information is relevant for a better understanding of the process on a molecular level but also for scale-up studies, *e.g*. for the design of pilot plants.

1. Introduction

The foreseen reduction in availability and the negative environmental impact of fossil feedstocks and products derived thereof have stimulated the search for renewable sources for the production of fuels and chemicals during the last decades. Biomass has been identified as an abundant source of renewable carbon that can be converted using a range of technologies to sustainable fuels and chemicals [1]. A successful example is the biodiesel (FAME) industry. The worldwide bio-diesel production has boomed since 2000 [2] and reached a level of over 30 billion liters in 2017 [3]. It is expected to increase to 41.9 billion liters in 2020 [4], because of the higher blending mandates released by many countries. This trend has led to a dramatic increase in the production of crude glycerol, a major by-product (*ca.* 10 wt.%) of the bio-diesel industry [5]. Glycerol is considered a very attractive green building block, which can be utilized to produce various bio-based chemicals [6]. Of the many options, the conversion of glycerol to bio-based aromatics (GTA, *e.g.*, benzene, toluene and xylenes, abbreviated as BTX) *via* catalytic pyrolysis approach is considered as an interesting option [7] and this approach has recently been reviewed by Muraza [3].

H-ZSM-5 based zeolites are among the most suitable catalysts for catalytic conversion of glycerol to BTX due to their unique three-dimensional micro-pore structure and high Brønsted acidity [3, 7]. However, the reported BTX yields over H-ZSM-5 are still rather low (Table 1), for instance, the carbon yield of total BTX was less than 8% in a very early report [7]. Several groups have focused on ZSM-5 modifications to improve catalyst performance with, for example, the introduction of (noble) metals (*e.g.,* Zn [8-10], Ga [8], Sn [10], Cu [8], Mo [8, 10], Ni [10], Ag [10], Pd [7, 11], and Pt [11]), dealumination [12], the use of hierarchical structures [13, 14] and the use of binders (*e.g.*, bentonite [15, 16]). In addition, co-feeding strategies, *e.g.*, with water [8, 17-19], alcohols [8, 18, 20], aromatics [21], alkanes [22], and vacuum gas oil [23], have also been explored to enhance the BTX yield.

Based on literature data, we can conclude that:

i) most studies are using diluted glycerol *e.g.*, with H_2O [17] and methanol [13], due to the fact that glycerol has a high viscosity (1.412 Pa·s) leading to challenges related to feeding in a micro-scale continuous-flow system.

ii) most studies are using an *in-situ* approach where both the pyrolysis step and catalytic conversion are performed simultaneously. However, an *ex-situ* approach where pyrolysis and catalytic upgrading are carried out in separate units allows for better control of process

conditions in the individual units. In addition, this approach is particularly advantageous when using glycerol contaminated with salts (*e.g*. crude glycerol [16]), which may result in excessive zeolite deactivation in case of an *in-situ* approach. In addition, an *ex-situ* approach also makes it possible to draw conclusions regarding the effect of the composition of the pyrolysis vapor on the performance in the catalytic aromatization reactor.

iii) most studies do not provide all relevant performance data in a comprehensive manner, like mass balance closures, activity *versus* time on stream, and activity profiles for catalysts after a substantial number of recycles. In addition, it is often unclear whether the peak yield of BTX is reported or the average yield over a certain runtime, which is of high relevance in case of severe catalyst deactivation. Also, effects of process conditions and level of catalyst deactivation on the distribution of the various BTX components have not been determined in detail. All this information is relevant for a better understanding of the process on a molecular level but also for scale-up studies, *e.g*. for the design of pilot plants.

iv) all studies reported so far (Table 1) were carried out at a wide range of reaction conditions (*e.g*., temperature, pressure and space velocity), which makes a comparison very cumbersome.

v) a very limited number of studies have reported on reaction pathways [7, 9, 10] and kinetics [24].

To the best of our knowledge there are no investigatiosn dealing with the conversion of pure glycerol to aromatics using a standard, unmodified H-ZSM-5 catalyst in a continuous set-up using an *ex-situ* approach. Recently, we [16] reported the catalytic pyrolysis of crude glycerol over a shaped ZSM-5/bentonite catalyst in a continuous bench-scale fixed bed reactor for bio-BTX synthesis at a scale of 200 g crude glycerol h^{-1} and obtained a BTX yield of 8.1 wt.% (14.6% on carbon basis). In this study, we report the *ex situ* pyrolysis of pure glycerol to BTX in a small scale (1 g h^{-1}) continuous set-up aiming to obtain detailed information on the performance of an unmodified H-ZSM-5(23) catalyst (activity, selectivity and stability) with time on stream (TOS). This includes determination of peak and overall BTX yields, mass, carbon and oxygen balances, the selectivity of the individual BTX components *versus* TOS, and assessment of the stability/lifetime of the catalyst, all aspects which are not disclosed in a comphrehensive manner in the existing literature (*vide supra*). An intermediate oxidative treatment was tested to regenerate the catalyst and five reaction/regeneration cycles were performed. Insights in catalyst deactivation mechanisms were obtained by detailed catalyst

Table 1. Performance of acidic catalysts for the conversion of pure glycerol to aromatics under various reaction conditions

T (°C)	P (bar)	WHSV (h^{-1})	Carrier gas	Catalyst	Glycerol conversion (%)	Benzene (C.%)*	Toluene (C.%)	Xylenes (C.%)	Total aromatics (C.%) or (wt.%)#	TOS	Remark	
400	20	2	H_2	H-ZSM-22	100	0	0	0	-	-	continuous fixed bed	Ref [7]
400	20	2	H_2	HNaMOR	92.9	0	0	0	-	-	reactor, 10 mm inner	
400	20	2	H_2	HY	95.2	0.3	0.9	1.9	-	-	diameter	
400	20	2	H_2	H-ZSM-5	95.1	1.2	2.6	3.6	-	-		
400	20	2	H_2	H-ZSM-5 + Pd/ZnO	99.0	0.7	5.6	11.8	-	-		
400	1	0.17	H_2	H-ZSM-5	90.2	0	0.8	9.0	-	-	continuous fixed bed	Ref [11]
400	1	0.17	H_2	Pt/H-ZSM-5	93.2	2.2	5.4	6.3	-	-	reactor, 0.3 mL	
400	1	0.17	H_2	Pd/H-ZSM-5	92.0	2.5	27.9	34.1	-	-	glycerol h^{-1}	
400	20.7	1	N_2	H-ZSM-5(23)	-	4.8	14.7	12.7	-	3 h		Ref [9]
400	20.7	1	N_2	H-ZSM-5(30)	-	6.8	19.7	16.5	-	3 h		
400	20.7	1	N_2	H-ZSM-5(50)	-	5.6	17.9	15.6	-	3 h		
400	20.7	1	N_2	H-ZSM-5(80)	-	4.5	14.9	15.2	-	3 h		
400	20.7	1	N_2	H-ZSM-5(280)	-	6.1	13.9	11.0	-	3 h		
400	20.7	1	N_2	Zn/H-ZSM-5(30)	-	10.0	35.3	20.1	-	3 h		
470	1.34	-	N_2	Al_2O_3	-	-	0.3	0.4	17 C.%	-	fixed bed reactor	Ref [22]
500	-	-	N_2	Y type FCC	-	-	-	-	12.7 C.%	30 s	microactivity test (MAT) reactor	Ref [25]
400	-	0.228	-	H-ZSM-5/bentonite	-	-	-	-	3.9 wt.%	-	continuous fixed bed	Ref [15]
400	-	0.228	-	Zn-ZSM-5/bentonite	-	-	-	-	12.2 wt.%	-	reactor	
400	-	0.228	-	Mn-ZSM-5/bentonite	-	-	-	-	6.4 wt.%	-		

*C.%: carbon basis yield; #wt.%: weight basis yield.

characterization studies on fresh, used and regenerated catalyst. Finally, the concentrations of a number of representative products were determined as a function of TOS and used to propose a reaction network for the GTA process. The results provide insights on molecular as well on a process level, which is essential for scale up of the GTA process.

2. Experimental Section

2.1. Chemicals

An ZSM-5 zeolite with a SiO_2/Al_2O_3 molar ratio of 23 (abbreviated as ZSM-5(23)) was obtained from Zeolyst International (product No. CBV2314) in the ammonia form. Glycerol (≥ 99.5%, CAS No. 56-91-5, denoted as pure glycerol), tetrahydrofuran (THF, analytical grade, CAS No. 109-99-9) and n-nonane (analytical grade, CAS No. 111-84-2) were supplied by Sigma-Aldrich. Liquid nitrogen and argon, technical grade nitrogen and synthetic air (N_2/O_2, 79/21 vol.%) gas were purchased from Linde.

2.2. Preparation of the H-ZSM-5(23) catalyst

The as-received ZSM-5(23) was converted from the ammonia-form to the H-form (*viz*., H-ZSM-5(23) by calcination at 600 °C for 8 h. The samples were subsequently pelletized using a bench-top pellet press (Model 4350, Carver Inc., die diameter of 13 mm) at 1 ton cm^{-2} pressure for 30 s. Thereafter, the samples were crushed manually (Agate mortar, IDL GmbH & Co. KG, part No. 210000100) and sieved (analytical sieves, Linker Industrie-Technik GmbH) in 3 fractions with different particle size ranges (212 - 300, 300 - 500 and 500 - 800 µm).

2.3. Catalytic conversion of pure glycerol via ex-situ catalytic pyrolysis

The *ex-situ* catalytic pyrolysis of pure glycerol was performed using a homemade set-up (CTMR-1, Figure 1).

Possible internal and external diffusion limitations were experimentally verified by varying the catalyst particle sizes (Figure S1) and the feed rate (Figure S2). When operating the unit at a glycerol flow rate > 1 g h^{-1} and a catalyst particle size < 500 µm, internal and external diffusion limitations were negligible and as such intrinsic kinetic data were obtained. The H-ZSM-5(23) catalyst (termed as Cat-F, 1.0 g) with particle size in the range of 300-500 µm was placed in the catalytic reactor (316 stainless steel, 10 × 1 mm, length = 200 mm, Swagelok, part No. SS-T10M-S-1.0M-6ME) and sandwiched between quartz wool (VWR

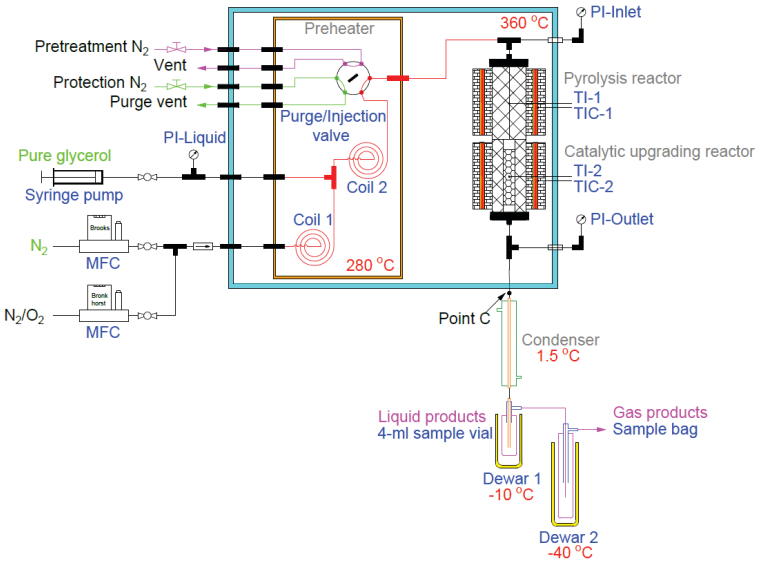

Figure 1. Schematic representation of the setup (CTMR-1) for the conversion of pure glycerol to aromatics.

international, part No. BEHRB00027716). The catalyst was pretreated *in-situ* using N_2 gas (1.8 ml min^{-1}, Swagelok, part No. SS-SS2-VH) at a preset temperature (500°C) with a temperature ramp of 6 °C min^{-1} (controlled by temperature controller, UR3274, Wachendorff Prozesstechnik GmbH & Co. KG) for 6 h. Glycerol was fed (1 g h^{-1}) to the preheater (280 °C, heated valve enclosure, VICI, part No. HVE6) by a syringe pump (NE-1010, Prosense B.V.) equipped with a syringe (50 ml gastight, Hamilton, part No. 85020). The N_2 feed (1.8 ml min^{-1}, controlled by a mass flow controller, GF040/0254A, Brooks) was preheated in Coil 1 (316 stainless steel, 1/16 × 0.014 inch, length = 1500 mm, Swagelok, part No. SS-T1-S-014-6ME). The preheated N_2 gas was combined with the glycerol feed and transferred via Coil 2 (same as Coil 1) to the purge vent. When the temperatures in the unit were at the pre-set values, the purge/injection valve (6-port 2-position high-temperature valve, VICI, part No. EH4C6WT) was switched and the feed stream (preheated N_2 and vaporized glycerol) was introduced to the pyrolysis reactor (same dimensions as catalytic reactor, filled with quartz wool, operated isothermally at 400 °C). The pyrolysis vapor was passed over the H-ZSM-5(23) catalyst in the

catalytic reactor and the products were subsequently condensed at 1.5 °C (controlled by the cooling thermostat ECO RE630, Lauda-Brinkmann, using ethanol as the coolant). The preheater, pyrolysis and catalytic units were operated at gauge pressures of 0 - 5 mbar. The pressures were measured using three pressure transducers (GFD/0254A, Brooks) placed in the glycerol feed line and before and after the pyrolysis/catalytic reactor. The liquid products were collected in sample vials (4 ml), which were positioned in a cylindrical KGW Dewar flask (Dewar 1, Fischer-Scientific, product code 10109560) containing liquid nitrogen. The temperature in the Dewar flask was monitored (Fischer-Scientific, product code 12363037) to maintain a temperature of the bottom of the sample vial of -10 ± 2 °C. Another condenser (immersed in Dewar 2 and operated at -40 ± 5 °C) was used to condense additional volatile products. Less than 1% of the target BTX products were collected in the second condenser, showing the effectiveness of the cooling system. The non-condensable gases were collected in the FlexFoil Plus sample bag (ProCare B.V., part No. 207023). The sample vials were changed every 20 min to collect the liquid products at different time on stream (TOS) (Figure S3). Gas phase products could not be accurately sampled during the time of stream due to interference with the collection of liquid samples. As such, additional experiments were performed without liquid sampling to collect all the gas phase products in one gas bag. In this case, all the liquid products were collected in sample vial (20-ml, Figure S4). Experiments with fresh catalysts were performed at least in duplicate.

2.4. Catalyst regeneration and reuse

The deactivated catalyst (termed as Cat-D) was *in-situ* regenerated in the catalytic reactor using an oxidative procedure with synthetic air (4 ml min^{-1}, controlled by mass flow controller, MRH 469/2, Bronkhorst, The Netherlands). The regeneration temperature was from room temperature to 700 °C with a temperature ramp of 1 °C min^{-1} and the regeneration step lasted for 12 h. After regeneration, the catalytic reactor was cooled to 500 °C and N_2 gas was re-introduced to the system. Simultaneously, pure glycerol and N_2 were preheated in the preheater to purge the preheating system. When the system was at steady state, the purge/injection valve was switched again to feed the pyrolysis/reactor system. The protocol for testing the regenerated catalysts was similar as the one for the fresh catalyst (Section 2.3). Totally, five regenerations were performed and four cycles of regeneration-reuse are

reported. The regenerated catalysts are denoted as Cat-Ri, where i stands for the number of regenerations.

2.5. Product analyses

The liquid products obtained at different TOS (Figure S3) were mixed with a stock solution of THF containing a known concentration of *n*-nonane (internal standard) to obtain homogenous samples. These samples were analyzed by a GC-MS (6890/5973, Hewlett-Packard, USA) using a Rtx-1701 column (Restek, USA, 30 m × 0.25 mm × 0.25 µm) to identify the products, and by a GC-FID (5890, Hewlett-Packard, USA) with the same column as the GC-MS to quantify the amounts of BTX. The weight- and carbon yields of BTX were calculated using Equations 1 and 2. The catalyst life-time is defined as the TOS when the BTX yield becomes negligible. The definitions for turnover number (TON), BTX productivity and selectivity of individual BTX components are given in Equations 3-5.

$$BTX\ mass\ yield\ (wt.\%) = \frac{weight\ of\ BTX\ product}{weight\ of\ Glycerol\ feed} \times 100 \quad (1)$$

$$BTX\ carbon\ yield\ (\%) = \frac{mol\ of\ carbon\ in\ BTX\ product}{mol\ of\ carbon\ in\ the\ glycerol\ feed} \times 100 \quad (2)$$

$$TON\ \left({}^{mol_{BTX}}/_{mol_{acid\ sites}}\right) = \frac{mol\ of\ BTX\ produced\ during\ life{-}time}{mol\ of\ Brönsted\ acid\ sites\ on\ fresh\ catalyst\ (Pyridine{-}IR\ analysis)} \quad (3)$$

$$BTX\ productivity\ \left({}^{mg_{BTX}}/_{g_{catalyst}}\right) = \frac{weight\ of\ BTX\ produced\ during\ life{-}time}{weight\ of\ catalyst\ loaded\ in\ the\ reactor} \quad (4)$$

$$BTX\ selectivity\ (\%) = \frac{mol\ of\ individual\ component\ formed}{total\ mol\ of\ BTX\ formed} \times 100 \quad (5)$$

To determine the mass-, carbon- and oxygen balances, the biphasic liquid products collected after a run (20 ml sample vials, Figure S4) were separated to obtain an aqueous and oil phase. The aromatics content (GC-FID, see above), the water content in the aqueous phase and oil phase were determined using a Karl-Fischer titration and the amount of carbon and hydrogen was determined by elemental analyses. Karl-Fischer titrations were performed using a 702 SM Titrino potentiometric titrator (Metrohm, Switzerland) using HYDRANAL™ 5 as the titer and HYDRANAL™ as the solvent (Honeywell, Germany). The elemental composition was determined using an elemental analyzer (EuroEA3000, Eurovector, Italy). The gaseous products in the gas bag were analyzed by GC-TCD (5890, Hewlett-Packard, USA)

using a CP-PoraBOND Q column (Varian, USA, 50 m × 0.53 mm × 10 µm,) and a HP-Molesieve column (Agilent, USA, 30 m x 0.53 mm x 50 µm,). The GC-TCD was calibrated using a reference gas (a mixture of C_1-C_3, CO, CO_2 and N_2, Westfalen AG, Germany, Product No. G322243) prior to analyses of the non-condensable gases.

2.6. Catalyst characterization

Before detailed characterization, the fresh and spent catalysts were ground into fine powders. Nitrogen isotherms were obtained at 77 K using an ASAP 2420 Surface Area and Porosity Analyzer. Before analyses, the samples were treated at 450 °C for 4 h to remove air. The Brunauer-Emmett-Teller (BET) method was used to determine the surface area by using the adsorption isotherms in the P/P_0 range of 0.05-0.25. The Barrett-Joyner-Halenda (BJH) method was used to calculate the meso-pore size distribution. The adsorption branch was used to avoid tensile strength effects, which are known to give an artifact at 4 nm in the pore size distribution [26]. The pore volume was calculated from the single point desorption at P/P_0 of 0.98. The ASAP 2420 Analyzer was also used for argon physisorption experiments (87 K). The free-space of each sample tube was determined according to the Micromeritics Application Note 104 prior to analyses. Before analyses, the catalysts were degassed at 450 °C for 4 h. The non-Localized Density Functional Theory method (Model # 251, Ar@87-Zeolites, H-form, NLDFT, Micromeritics) was used to determine the micro-pore size distribution and micro-pore volume.

A D8 Advance Powder Diffractometer with Cu Kα radiation (λ= 1.5418 Å) operated at 40 kV and 40 mA was used acquire X-Ray Diffraction (XRD) patterns. A LYNXEYE detector (1D mode) using a 2θ scan range of 5 - 50° was used. The relative crystallinity of the samples was calculated using Equation 6 (ASTM D5758-01). It involves a comparison of the peak height of the 2θ reflection at 24.37° of the actual catalyst sample ($H_{Catalyst}$) with that of pristine H-ZSM-5(23) ($H_{H\text{-}ZSM\text{-}5(23)}$).

$$Relative\ crystallinity\ (\%) = \frac{H_{catalyst}}{H_{H-ZSM-5(23)}} \times 100 \quad (6)$$

The morphology and local elemental composition of the catalysts were obtained using a Tecnai T20 Transmission Electron Microscope with a Gatan 2k x 2k CCD camera and operated at 200 keV. An X-Max T80 SDD Energy Dispersive X-ray Detector was used. Prior to analyses,

the samples were dispersed in ethanol using an ultrasonic bath and subsequently deposited on a copper grid coated with carbon.

An Optima 7000 DV Optical Emission Spectrometer was used to perform Inductively Coupled Plasma Atomic Emission Spectroscopy (ICP-AES). Prior to analyses, the samples were dissolved in 3 wt.% HF in water by stirring overnight at room temperature.

An AV-I 750 MHz spectrometer operated at 17.6 Tesla was used to perform magic angle spinning solid state nuclear magnetic resonance (MAS ssNMR). The samples were placed in zirconium rotors (4-mm) and the spectra were recorded at a spin rate of 54.74. In this magnetic field, the ^{27}Al and ^{29}Si nuclei resonate at 195.47 and 149.05 MHz. Additional data for ^{27}Al MAS ssNMR: chemical shifts were referenced using $Al(NO_3)_3$; an excitation pulse of 0.5 µs was used combined with a recycling delay of 1 s, 1024 scans. Data were processed using a line broadening function (50 Hz) and baseline correction. Additional data for ^{29}Si MAS ssNMR spectra: chemical shifts were referenced to tetramethylsilane (TMS), an excitation pulse of 2 µs was used with a recycling delay of 1 s, 1024 scans were acquired. Data processing involved a line broadening function (100 Hz) and an additional baseline correction. All the NMR spectra were processed in appropriate software packages (Topspin 3.2 and MestReNova).

Pyridine-IR measurements were carried out using a Nicolet 6700 FT-IR spectrometer equipped with an tailor-made cell. The sample (ca. 50 mg) was placed in a die (10 mm diameter) and pressed for 5 s at 3 ton cm^{-2} pressure. The sample was placed in the sample holder and preheated under vacuum (< 10^{-3} bar) to 350 °C. The sample was allowed to equilibrate for 4 h. After cooling to 25 °C, pyridine was introduced, the sample was evacuated at 150 °C for 30 min and cooled to 25 °C to record an IR spectrum. An AutoChem II 2920 was used to determine the total acidity of the catalyst using ammonia (NH_3-TPD). The sample was placed in the device at 550 °C under a He flow (50 ml min^{-1}, 1 h) and then cooled (100 °C). Ammonia in He (1.0 vol.%, 50 ml min^{-1}) was introduced and the catalyst was saturated with ammonia for 1 h. Afterwards, the sample was purged using He gas (50 ml min^{-1}) to desorb weakly adsorbed ammonia. Finally, the sample was heated to 550 °C using a temperature ramp of 10 °C min^{-1} to desorb the remaining ammonia. A TCD calibrated for NH_3 was used to quantify desorbed products.

A TGA 4000 Analyzer (PerkinElmer) was used to obtain thermogravimetric data. The catalysts were placed in ceramic crucibles, which were heated from 50 °C to 800 °C

(temperature ramp of 10 °C min^{-1}) under a flow of air (50 ml min^{-1}). TGA of empty ceramic crucibles were also performed to compensate for matrix effects of the crucibles.

The amounts of carbon and hydrogen on the deactivated catalysts were determined using an elemental analyzer (EuroEA3000, Eurovector, Italy). The amount of hydrogen was corrected for adsorbed water. The latter amount was taken as the weight loss of the sample in TGA in the temperature range of 50 - 300 °C. Average values of two analyses are reported.

3. Results and discussions

An *ex-situ* catalytic pyrolysis approach for the conversion of pure glycerol to bio-aromatics was investigated, involving glycerol vaporization/pyrolysis in a pyrolysis reactor followed by the catalytic upgrading of the pyrolysis vapor over an H-ZSM-5 catalyst in the catalytic upgrading reactor. Initially, preliminary experiments on the non-catalytic pyrolysis of pure glycerol were performed to determine the composition of the pyrolysis vapor, followed by extensive studies in the integrated unit with catalyst present.

3.1. Pyrolysis of pure glycerol

Pyrolysis of pure glycerol was performed in the CTMR-1 unit (Figure 1), where both the pyrolysis and catalytic upgrading section were filled with quartz wool. Reaction conditions were as follows: pyrolysis reactor temperature of 400 °C, catalytic upgrading reactor temperature of 500 °C, atmospheric pressure, N_2 flow of 1.8 ml min^{-1}, and a TOS of 3 h. The vapor products were condensed and three liquid samples (yield of 81.7±1.4 wt.%) were collected every hour. The water content in the samples (Karl-Fischer titration) was 14.3±0.3 wt.% due to dehydration of glycerol and intermediates thereof under thermal pyrolysis conditions [27, 28]. This corresponds to a water yield 11.7 ± 0.1 wt.% on glycerol. GC-MS analysis of the liquid product indicates that glycerol was partly converted to a variety of oxygenates, including acetaldehyde, acrolein, acetol, 2-propen-1-ol, glycolaldehyde, 1,2-ethanediol, glycidol, propane-1,2-diol and diethoxymethane, in line with literature data [27-29] for pyrolysis of glycerol at various temperatures and weight hourly space velocities. It should be noted that the pyrolysis of glycerol affords a mixture of reactive intermediates that might further react (*e.g.*, Michael additions, aldol condensations) during condensation in the cooling section of the unit, and as such the composition of the vapor phase after pyrolysis is not necessary exactly similar to the condensed liquid phase.

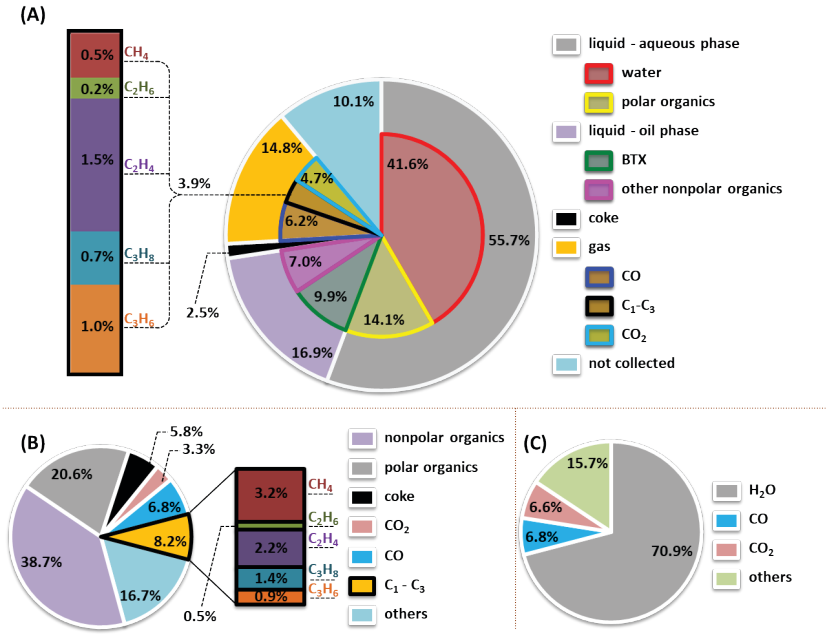

Figure 2. (A) mass balance, (B) carbon balance and (C) oxygen balance for catalytic conversion of pure glycerol to BTX over fresh H-ZSM-5(23). Reaction condition: pyrolysis temperature of 400 °C, aromatization temperature of 500 °C, atmospheric pressure, N_2 flow of 1.8 ml min^{-1}, H-ZSM-5(23) (300 - 500 µm, 1 g loading), WHSV of 1 h^{-1} and TOS of 5 h.

3.2. Ex-situ catalytic pyrolysis of pure glycerol over an un-modified H-ZSM-5(23) zeolite

The conversion of pure glycerol to aromatics *via* an *ex-situ* catalytic pyrolysis approach using an unmodified H-ZSM-5(23) zeolite was also performed in the CTMR-1 unit (Figure 1) with a pyrolysis and a catalytic (aromatization) section. The results for a representative experiment at a pyrolysis temperature of 400 °C, aromatization temperature of 500 °C with an unmodified H-ZSM-5(23) (300 - 500 µm, 1 g loading) catalyst, a WHSV of 1 h^{-1} and a TOS of 5 h are given in Figure 2. These conditions were selected based on preliminary screening experiments.

Satisfactorily total mass balance (89.9%, Figure 2-A), carbon balance (83.3%, Figure 2-B) and oxygen balance closures (84.3%, Figure 2-C) were achieved. The primary product phases are a biphasic liquid (72.6 wt.%), gas-phase components (14.8 wt.%), and coke deposits on

the catalyst (2.5 wt.%, 5.8% carbon yield). The remainder (10.1 wt.% by difference) is likely the solids deposited on the walls of the pyrolysis reactor, condensers and transfer lines, which could not be recovered. The aqueous phase (55.7 wt.%) consists mainly of water (41.6 wt.%), the remainder being polar organics (14.1 wt.%, carbon yield of 20.6%) such as acrolein and acetaldehyde and a trace amount of unconverted glycerol (proved by GC-MS). The oil phase (16.9 wt.%, 38.7% carbon yield) contains the desired BTX (9.9 wt.%, 23.1% carbon yield) and higher aromatics (7.0 wt.%, *e.g.*, naphthalene and substituted naphthalenes). Major gaseous products are CO (6.8% carbon yield), CO_2 (3.3%, carbon yield), and light hydrocarbons (C_1-C_3, 8.2 % carbon yield).

The oxygen balance shows that most oxygen from glycerol (70.9%) is converted to water, indicating that dehydration is the main pathway for the deoxygenation of glycerol over H-ZSM-5(23). This water is both formed in the pyrolysis unit (about 30%, see Section 3.1), as well as in the catalytic upgrading reactor (about 70%). Decarboxylation and decarbonylation reactions are responsible for the conversion of only 13% of the bound oxygen in glycerol.

To analyze the evolution of the BTX yield with time on stream, the liquid products were collected every 20 min during the run (Figure S3). The initial samples consist of two immiscible and transparent liquid phases (water and organic phase with BTX, *e.g.*, samples 1 - 7, Figure S3). At this stage, glycerol conversion is quantitative. At extended times on stream, the product samples became cloudy single-phase light brown liquids (*e.g.*, Samples 8 - 9, Figure S3) with substantially lower BTX amounts (Figure S5). At longer run times, further homogenization and darkening of the liquid products was observed (*e.g.*, Samples 10 - 13, Figure S3). Here, glycerol conversion is not quantitative anymore, main products are oxygenates (*vide infra*) and BTX is not detected. Thus, the formation of a homogeneous liquid product phase is a good indication for severe catalyst deactivation. Therefore, subsequent experiments were performed until a monophasic product was formed (*e.g.*, Sample 9, Figure S3) to prevent clogging due to the formation of solids in the line between the reactor and condenser (Point C, Figure 1).

The total BTX yield and the yield of individual BTX components are given in Figures 3 (yield on carbon basis) and S6 (yield on weight basis). In the initial stage, the yields increase due to start-up of the reactor. After about 50 min, the maximum BTX yield is reached, and this yield is maintained till about 150 min. Thereafter, the BTX yield drops and after *ca*. 300 min, BTX is not detected anymore in the liquid product, indicating that the catalyst is fully deactivated.

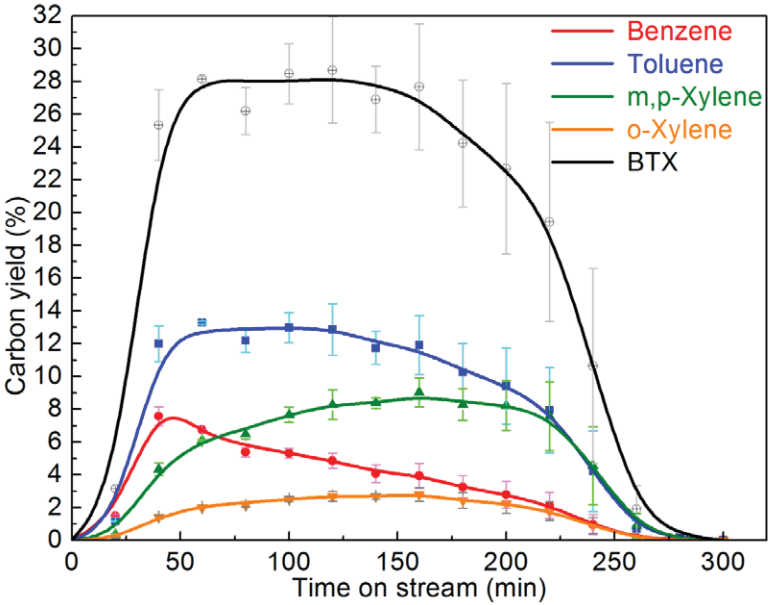

Figure 3. Carbon yield of the total and individual BTX *versus* TOS. Reaction conditions: pyrolysis temperature of 400 °C, aromatization temperature of 500 °C, atmospheric pressure, N_2 flow of 1.8 ml min^{-1}, H-ZSM-5(23), (300 - 500 µm, 1 g loading), and WHSV of pure glycerol of 1 h^{-1}.

The peak yield of BTX was 28.1 ± 0.2% on carbon basis (12.1 ± 0.1 wt.% on weight basis). This yield is considerably higher than those reported for the catalytic conversion of glycerol over H-ZSM-5 catalysts *via* an *in-situ* approach [7, 14] and using H_2 as a co-feed [11] (Table 1) and is the best performance for an un-modified H-ZSM-5 catalyst reported so far. The BTX productivity was 398 ± 55 mg BTX g^{-1} catalyst corresponding to a TON of 13.6 ± 1.9 mol BTX mol^{-1} acid sites. The selectivity's of the individual BTX were 21.5±0.3% (benzene), 45.0±0.2% (toluene), 25.8±0.0% (m,p-xylene) and 7.7±0.1% (o-xylene), respectively.

3.3. Catalyst regeneration-reaction cycles

In the previous paragraph, it was shown that the H-ZSM-5(23) zeolite becomes inactive after 300-min TOS (Figure 3) under the prevailing reaction conditions. Analyses of the spent catalyst by various techniques (*vide infra*) show that the main cause for deactivation is coke

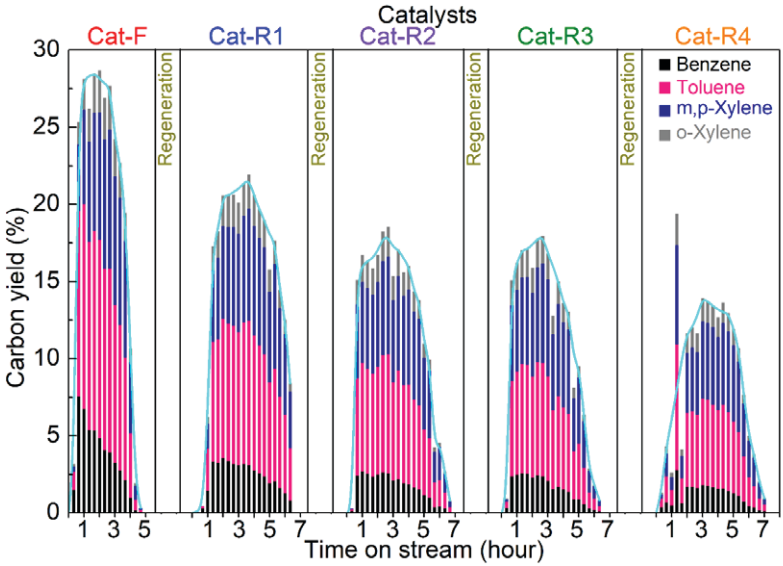

Figure 4. Yields of BTX over the fresh and regenerated H-ZSM-5(23) catalysts *versus* TOS. Reaction conditions: pyrolysis at 400 °C, aromatization at 500 °C, atmospheric pressure, N_2 flow of 1.8 ml min^{-1}, H-ZSM-5(23) (300 - 500 µm, 1 g catalyst loading), and WHSV of 1 h^{-1}.

deposition on the catalyst (12.0 wt.%, Figure S7), leading to a blockage of the micro-pores [7, 10, 16, 30]. TGA data for the spent catalyst (Figure S7) show that the minimum temperature required to remove the coke by air oxidation is about 615 °C. The required time to remove all the coke on the catalyst at 700 °C was estimated to be about 12 h, considering that the coke removal rate at 700 °C was estimated as 1.1 wt.% h^{-1} (Figure S7). The latter was confirmed by several regeneration trails performed at 650 and 700 °C for 4 - 12 h. Based on these experiments, the deactivated H-ZSM-5(23) (Cat-D) was *in-situ* regenerated in the reactor at 700 °C for 12 h by using air. Subsequently the regenerated catalyst was tested using the same protocol as for the fresh catalyst. In total, 4 regeneration-reaction cycles were performed and the BTX yields *versus* TOS over the regenerated catalysts are shown in Figures 4 and S8.

The BTX peak yield for the regenerated catalysts decreased significantly (*e.g.*, 28.1% for Cat-F *vs.* 13.9% for Cat-R4, yield on carbon basis) with the number of regeneration-reaction cycles (Figure 5). This decreased catalyst activity is also reflected in a reduction in the total BTX productivity (*e.g.*, 398 mg BTX g^{-1} for Cat-F *vs*. 270 mg BTX g^{-1} for Cat-R4, Figure 5). For

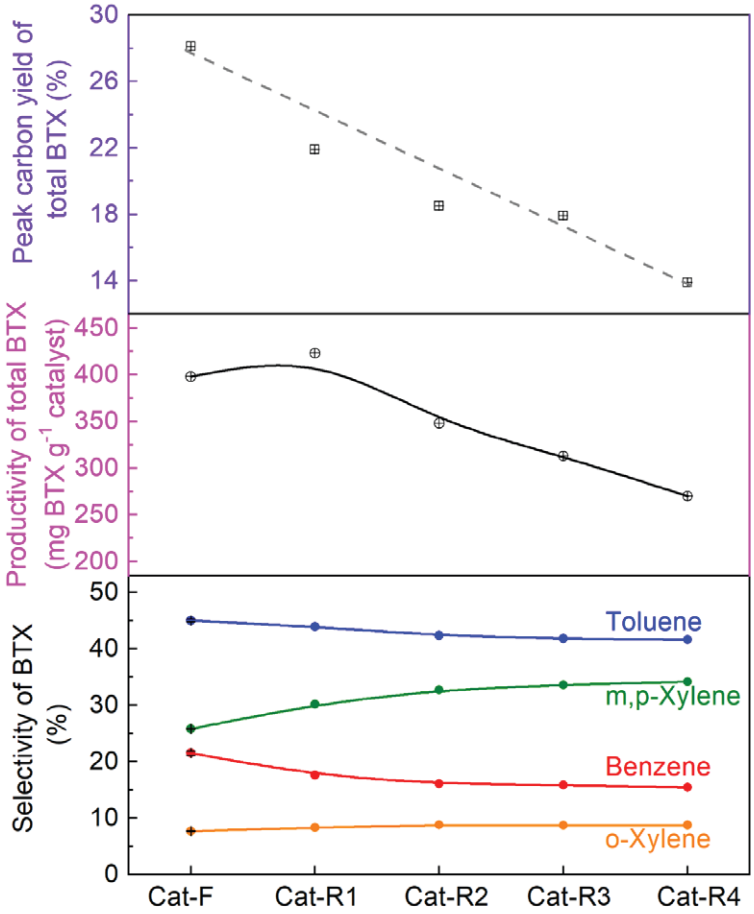

Figure 5. Peak carbon yield and productivity of total BTX, and selectivity of BTX over the fresh and regenerated H-ZSM-5(23) catalysts. Reaction conditions: pyrolysis at 400 °C, catalytic upgrading at 500 °C, atmospheric pressure, N_2 flow of 1.8 ml min^{-1}, H-ZSM-5(23) particle size of 300 - 500 µm, loading of H-ZSM-5(23) zeolite of 1 g, and WHSV of 1 h^{-1}.

each regeneration cycle, the BTX productivity is reduced with about 15% (Figure 5). Of interest is the prolonged catalyst life-time (*e.g.*, 300 min for Cat-F *vs*. 420 min for Cat-R for 1 g catalyst loading, Figures 4 and S8), which suggests a change in the amount and type of catalytically

active species during recycles (*vide infra*). The recycle/regeneration experiments clearly indicate that both reversible and irreversible deactivation of the H-ZSM-5(23) catalyst occurs.

The selectivity to individual BTX components also changes as a function of the number of regeneration-reaction cycles. Particularly, the selectivity to m,p-xylene increases at the expense of benzene and toluene (Figure 5). This points to a change in catalyst structure upon recycle/regeneration, which was indeed confirmed by detailed catalyst characterization studies (*vide infra)*.

3.4. Catalyst characterizations for the fresh, deactivated and regenerated H-ZSM-5(23) catalysts

To get insights in the irreversible deactivation of H-ZSM-5(23), the fresh catalyst (Cat-F), deactivated catalyst after the first reaction (Cat-D), and regenerated catalysts after the first regeneration (Cat-R1) and fifth regeneration (Cat-R5) were characterized in details using a range of techniques. An overview of relevant data is given in Table 2.

3.4.1. Textural properties

The N_2 isotherms for the fresh H-ZSM-5(23) and regenerated catalysts (Figure S9-A-a, c and d) show typical type I (at low P/P_0) and type IV (at higher P/P_0) isotherms [31, 32], indicating the presence of micro-pores and inter-crystalline voids [33, 34]. The pore size distribution (PSD) of the meso-pores in fresh H-ZSM-5 zeolite was determined using the BJH approach and the results are in agreement with literature data [16, 33, 35]. However, data on the PSD for the micro-pores in H-ZSM-5 are hardly reported. Additional low-pressure Ar adsorption experiments were performed at 87 K and analyzed using the NLDFT method (Section 2.6) to calculate the micro-pore size distribution and volume of pristine H-ZSM-5(23). The micro-pore volume was calculated at 0.20 $cm^3\ g^{-1}$, which is *ca*. 95% of the total pore volume, confirming the highly microporous structure of the H-ZSM-5 zeolite. When combining the physisorption data using N_2 and Ar, the PSD of the micro- and meso-pores of H-ZSM-5(23) show a BJH meso-pore size distribution (< 5 nm with a peak maximum at 3.8 nm, Figure S9-B-a, c and d) and a NLDFT micro-pore size distribution (0.45 - 0.6 nm and centered at 0.52 nm, Figure S9-C-a, c and d). Two artifacts are present in the NLDFT micro-pore size distribution of the pristine H-ZSM-5(23) (Figure S9-C-a), a PSD centered at 0.92 nm (attributed to *fluid-to-crystalline* phase transition of the adsorbent [26] in the micro-pores at P/P_0 of 10^{-3}) and a PSD

Table 2. Characterization of the fresh, used, and regenerated catalysts

Catalyst	SiO_2/Al_2O_3[a] (mol:mol)	SiO_2/Al_2O_3[b] (mol:mol)	I_{EFAl}/I_{FAl}[c]	S_{BET}[d] ($m^2\ g^{-1}$)	V_{pore}[d] ($cm^3\ g^{-1}$)	$V_{micropore}$[e] ($cm^3\ g^{-1}$)	B-Py (1545)[f] (mmol pyridine g^{-1} sample)	L-Py (1455)[f] (mmol pyridine g^{-1} sample)	B/L[f]	Acidity[g] (mmol $NH_3\ g^{-1}$ sample)	Relative crystallinity[h]
Fresh (Cat-F)	22.2	23.1	0.1	371	0.21	0.20	0.3128	0.1110	2.8	1.464	100
Deactivated (Cat-D)	23.7	24.9	0.4	10	0.02	0.005	n.d.	n.d.	-	0.131	-
1st Regenerated (Cat-R1)	24.8	25.4	0.5	308	0.19	0.18	0.0665	0.0632	1.1	0.516	90.2
5th Regenerated (Cat-R5)	25.1	27.0	0.6	339	0.18	0.17	0.0347	0.0329	1.1	0.281	86.8

[a]ICP-AES, [b]TEM-EDX, [c]MAS ssNMR, [d]N_2 adsorption-desorption, [e]Ar adsorption-desorption, [f]Pyridine-IR, [g]NH_3-TPD, [h]XRD, and n.d. = not detectable.

smaller than 0.45 nm (resulted from the inflection observed at p/p_0 of 10^{-5}, which is likely related to another phase-transition or mono-to-multilayer coverage of the pores).

For the deactivated catalyst (Cat-D), the N_2 adsorption-desorption isotherms (Figure S9-A-b) resemblance a type III isotherm [31], indicating that the pores of H-ZSM-5(23) are completely blocked by coke deposition. This is confirmed by the BJH meso-pore size (Figure S9-B-b) and NLDFT micro-pore size distribution (Figure S9-C-b). Consequently, the specific surface area, total pore volume and micro-pore volume of Cat-D decreased considerably to 3.2%, 9.5% and 2.5%, respectively, compared to those for Cat-F (Table 2). Upon *in-situ* oxidative regeneration, the micro-porosity was restored, as is evident from the NLDFT micro-pore size distribution of Cat-R1 and Cat-R5 (Figure S9-C-c and d). However, the specific surface area, total pore volume and micro-pore volume for the regenerated catalysts were reduced progressively upon regeneration (Table 2) to *ca*. 85 - 90% of the value for fresh H-ZSM-5(23) after 5 regenerations. This indicates a change in the H-ZSM-5 framework during the reaction - regeneration cycles, confirmed by HR-TEM-EDX and ^{27}Al and ^{29}Si MAS ssNMR (*vide infra*).

3.4.2. Crystal structure

The XRD patterns of the fresh, deactivated and regenerated catalysts (Figure S10) show typical features of the highly crystalline MFI-type zeolite[36, 37]. Clear diffraction peaks from the crystalline ZSM-5 structure are present at 2θ= 7.9° and 8.9° (♥), corresponding to the [011] and [200] planes [38]. The XRD pattern of Cat-D (Figure S10-b) displays additional features when compared to fresh ZSM-5. The intensity of the diffraction peaks (♦) at 2θ = 13.16°, 16.46°, 23.66°, 25.52° and 29.95°, assigned to [002], [212], [151], [323] and [062] planes, respectively, is greatly reduced compared to that for Cat-F. Concurrently, three new diffraction peaks (∇) at 2θ = 23.15°, 26.70° and 45.29° appear and overlap with the twin diffraction peaks (•) at 2θ = 23.05° and 23.21°, 26.56° and 26.83°, and 45.02° and 45.41° (assigned to [501] and [051], [004] and [104], and [0100] and [1000] planes of pristine H-ZSM-5, respectively). Both observations are indicative for deposition of coke on Cat-D with a high crystallinity [16], confirmed by comparing the XRD spectra after oxidative regeneration (Figure S10-c and d).

The two regenerated catalysts (Cat-R1 and Cat-R5) show the same XRD patterns as Cat-F. However, the relative crystallinity of the catalysts is reduced with each regeneration step to *ca*. 87% of that of the fresh H-ZSM-5(23) zeolite after 5 regenerations (Table 2). This is in good

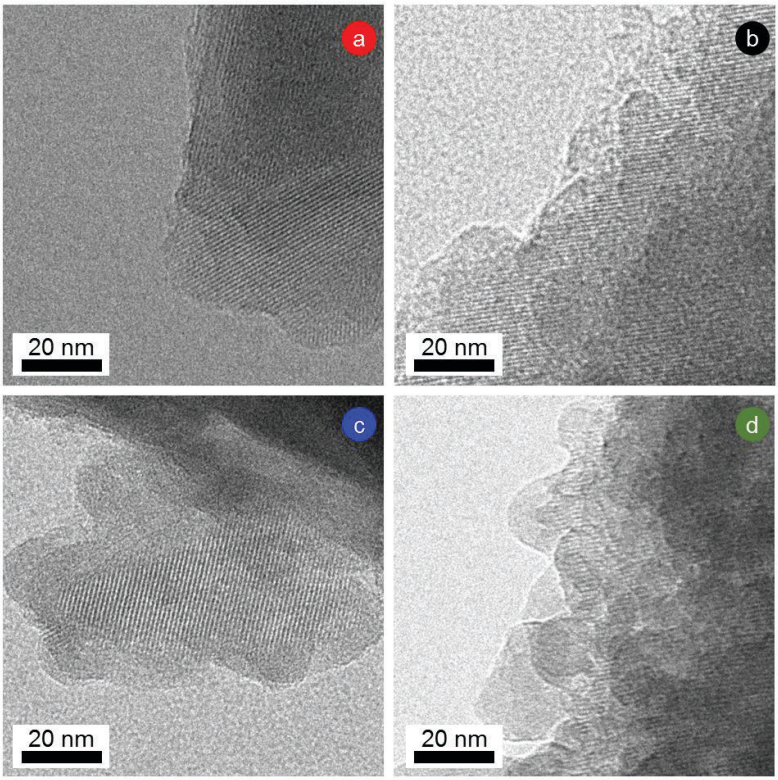

Figure 6. TEM images of (a) Cat-F, (b) Cat-D, (c) Cat-R1, and (d) Cat-R5.

accordance with N_2 and Ar physorption data, indicating a slight disruption of the H-ZSM-5 framework during the reaction - regeneration cycles, leading to a decrease in specific surface area and micro-porosity.

3.4.3. Morphology

A high resolution TEM image of fresh H-ZSM-5(23) particles (Figure 6-a) shows a highly ordered structure, which is consistent with literature data [39] and the XRD results (Figure S10-a). The lattice fringe is still visible for Cat-D (Figure 6-b), despite the fact that the surface and micro-pores of Cat-D are covered with coke. This indicates that the deactivated catalyst still has a high crystallinity, in line with the XRD results (Figure S10-b). Besides, an amorphous edge on the Cat-D particles is present (Figure 6-b), likely arising from deposited coke with a

lower crystallinity than H-ZSM-5. The HR-TEM images of the regenerated catalysts do not show a clear lattice fringe on the edges of the H-ZSM-5 particles, indicating a (partial) collapse of H-ZSM-5 crystalline structure after reaction - regeneration cycles. In line with this is a reduction in the relative crystallinity for Cat-R1 and Cat-R5 compared to the fresh catalyst (Table 2). The observed disruption in the H-ZSM-5 morphology might be due to dealumination of the zeolite framework [40] resulting from a high-temperature exposure to steam produced during reaction and the oxidative regeneration cycles to remove coke.

The observed dealumination of the H-ZSM-5 framework in the regenerated catalysts is confirmed by energy dispersive X-ray (EDX) mapping, see Table 2 for details). The overall SiO_2/Al_2O_3 molar ratio for the four samples increases with the number of reaction - regeneration cycles, indicating dealumination in the H-ZSM-5 particles. This was confirmed by ICP-AES analysis for the four catalysts, which also shows that the SiO_2/Al_2O_3 molar ratio of the bulk catalyst increases with increasing number of regeneration cycles (Table 2). In addition, the distribution of Si and Al within a H-ZSM-5 particle also changes as a function of reaction-regeneration cycles. The elemental map of Cat-F (Figure 7-a) shows a uniform distribution of Al and Si. However, Al is slightly agglomerated in Cat-D (Figure 7-b), which becomes more pronounced in the element maps for the regenerated catalysts (Figure 7-c and d). For Cat-R1 and Cat-R5, the amount of Al is higher on the edges of the H-ZSM-5 particles, in accordance with the amorphous edge observed in the corresponding HR-TEM images (Figure 6-c and d).

3.4.4. Framework

To further investigate the changes in the H-ZSM-5 framework upon reaction-regeneration, ^{27}Al and ^{29}Si MAS ssNMR analyses were performed. The ^{29}Si MAS ssNMR spectra of the four catalysts (Figure 8-B) show a peak centered at δ= -113 ppm, associated with one of the Q^4 linkages of silicon (Si(4Si, 0Al), and a shoulder at δ= -106 ppm, corresponding to the Si(3Si, 1Al) linkage [41, 42] in the framework of H-ZSM-5. The intensity of the shoulder significantly decreases after coke deposition (Figure 8-B-b) and slowly disappears with an increase in the number of regeneration - reaction cycles (Figure 8-B-c and d). This decrease in the amount of Q^4(3Si, 1Al) linkages is indicative for the occurrence of dealumination.

The ^{27}Al MAS ssNMR spectra of Cat-F (Figure 8-A-a) show peaks at δ= 53 ppm attributed to aluminum atoms with a tetrahedral coordination (FAl) and one at δ= 0 ppm from extra-framework aluminum atoms (EFAl, $Al(OH)_3$) in an octahedral arrangement [43]. The EFAl to

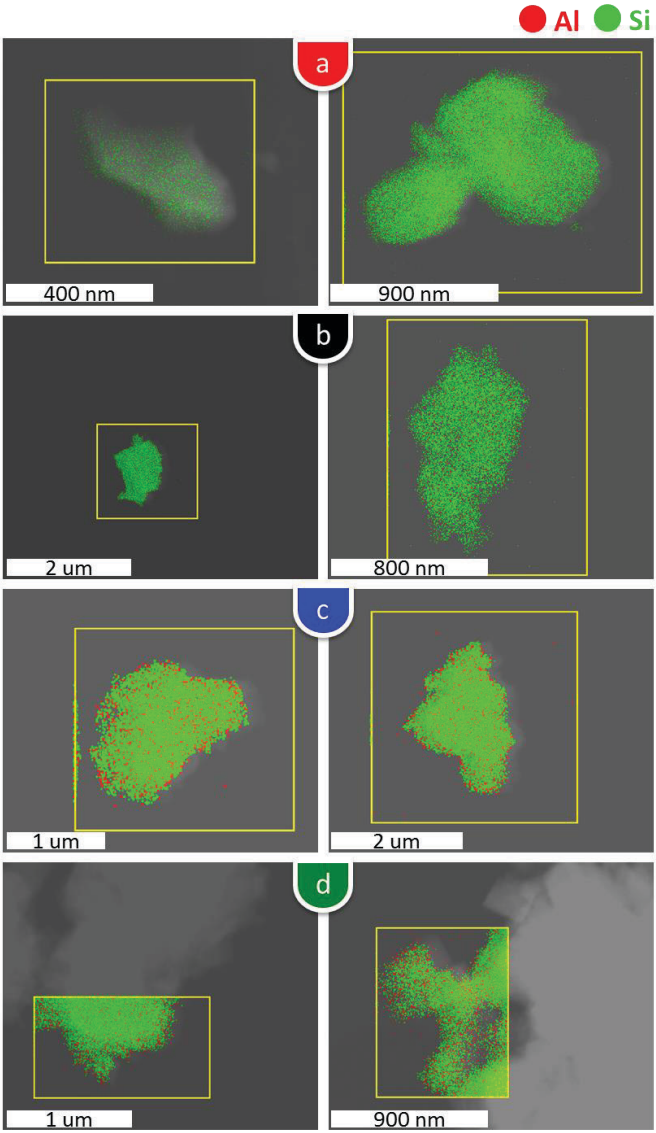

Figure 7. Al and Si maps in (a) Cat-F, (b) Cat-D, (c) Cat-R1, and (d) Cat-R5.

FAL peak intensity ratio (I_{EFAl}/I_{FAl}) for the two regenerated catalysts (Cat-R1 and Cat-R5) is markedly different (Table 2), indicating that during the reaction - regeneration cycles, FAl is

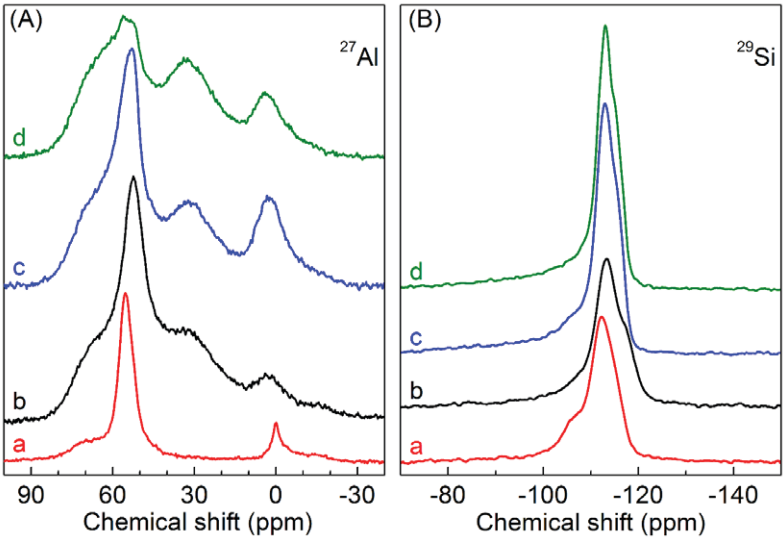

Figure 8. ^{27}Al (A) and ^{29}Si (B) MAS ssNMR spectra of (a) Cat-F, (b) Cat-D, (c) Cat-R1, and (d) Cat-R5.

converted to the thermodynamically favored EFAl [40]. This is confirmed by formation of a peak centered at δ= 30 ppm in the ^{27}Al MAS ssNMR spectra for the deactivated and regenerated catalysts (Figure 8-A-b, c and d), as a consequence of the formation of 5-coordinated extra-framework aluminum species [42]. These are known to be formed by the interaction of EFAl species with the Brønsted acid sites. This suggest that the amorphous edges observed in the TEM images of the deactivated and regenerated catalysts may be related to the formation of 5- and 6-coordinated extra-framework aluminum species.

Of interest is the observation of a significantly increased I_{EFAl}/I_{FAl} ratio for Cat D (Table 2). Comparatively, subsequent reaction - regeneration cycles have a by far lower impact on the I_{EFAl}/I_{FAl} ratio These observations indicate that dealumination of the H-ZSM-5 framework mainly occurs during *ex-situ* catalytic pyrolysis of glycerol and not during catalyst regeneration in air. A possible explanation is the involvement of water in the form of steam (Figure 2) in the dealumination process, which is generated in significant amounts by the dehydration of glycerol and the intermediates formed thereof. Part of the water is formed already in the pyrolysis step, meaning that the feed to the catalytic upgrading reactor already contains

significant amounts of water, which is expected to have a major effect on the catalyst structure in the initial part of the bed.

3.4.5 Acidity

Pyridine-IR spectra of fresh and regenerated H-ZSM-5 catalysts (Figure S11-a, c and d) show three bands at 1545 cm^{-1}, 1490 cm^{-1} and 1455 cm^{-1}, corresponding to C-CN vibrations of protonated pyridine (B-Py), H-bonded pyridine (H-Py) and metal coordinated pyridine (L-Py), separately [44]. The bands at 1545 cm^{-1} and 1455 cm^{-1} were used to calculate the amounts of Brønsted and Lewis acidic sites in fresh and regenerated H-ZSM-5 catalysts (Table 2) [45, 46]. The pyridine-IR acidity measurement reveal that the acidity of the regenerated catalysts is reduced considerably compared to the fresh H-ZSM-5. In addition, the data also indicate that the number of Brønsted acid sites is reduced much faster than the number of Lewis acid sites with the number of reaction - regeneration cycles. The acidity of Cat-D is not detectable by pyridine-IR measurement, likely due to the fact that the surface of Cat-D is completely covered by coke. Accordingly, additional NH_3-TPD analysis was performed. The NH_3-TPD curve of Cat-F (Figure S12-a) shows a peak with a maximum at 210 °C, associated with weak acid sites, and one at 420 °C, associated with strong acid sites for a ZSM-5 zeolite [38, 47]. Cat-D shows no Brønsted acidity, in agreement with the pyridine-IR measurement (Figure S12-b). Furthermore, most of the Brønsted acid sites are deactivated (*ca*. 79% loss) during the first reaction - regeneration cycle, compared to 11% loss of Brønsted acidity in the subsequent 4 reaction - regeneration cycles (Table 2). The loss in acidity of H-ZSM-5 during the first reaction - regeneration cycle is substantially higher than the reported values for a temperature treatment only, *e.g.*, *ca*. 55% loss of Brønsted acidity after calcination at 700 °C [40]. This indicates that most of the dealumination of the H-ZSM-5 framework occurs during the catalytic conversion of the glycerol pyrolysis vapor, in agreement with the observation that the changes in the I_{EFAl}/I_{FAl} ratio was considerably higher for Cat-D as compared to Cat-F (Section 3.3.4).

3.4.6 Discussion

Initial catalyst deactivation when using a fresh catalyst is mainly the result of coke deposition on the catalyst. On Cat-D, the amount of coke was about 12.0 wt.%, which covers *ca*. 96.8% of the surface area, *ca*. 97.5% of micro-pores volume and all of the Brønsted acid sites (Scheme 1), and this leads to complete deactivation of the catalyst after 300-min TOS. During reaction (and subsequent regeneration as well), aluminum from the H-ZSM-5

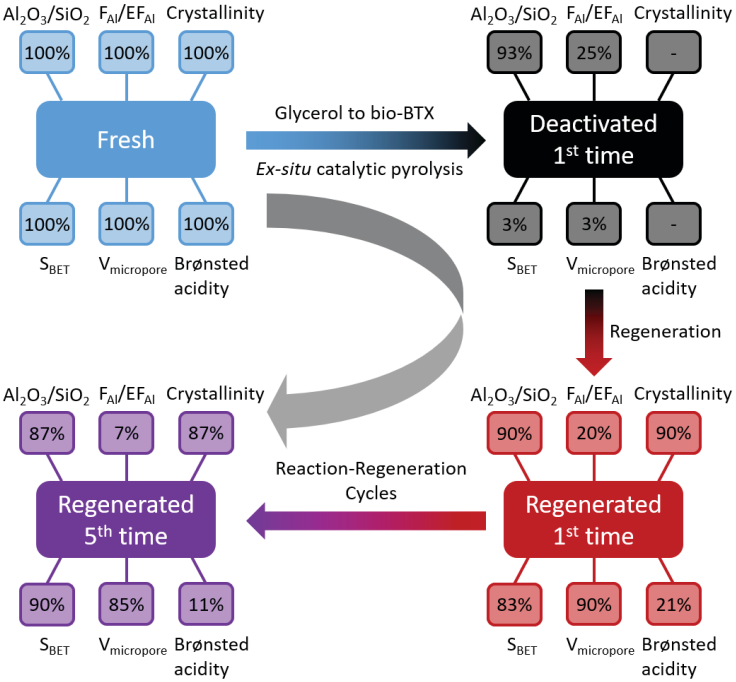

Scheme 1. Relevant changes in H-ZSM-5(23) properties during reaction-regeneration cycles.

framework is transferred to extra-framework positions, particularly at the external surface of a catalyst particle, forming new 5-coordinated aluminum species [48]. This extra-framework aluminum might subsequently migrate from the H-ZSM-5 particles, leading to a slightly increased SiO_2/Al_2O_3 molar ratio for the deactivated and regenerated catalysts and as such result in dealumination of the H-ZSM-5 framework [49]. Dealumination of the framework causes structural damage (resulting in decreased microporosity and crystallinity) and a decrease in acidity. As such, though the coke can be completely removed by an *in-situ* regeneration of Cat-D using air, the surface area, micro-pore volume, relatively crystallinity and Brønsted acidity of Cat-R1 are only recovered partly, to *ca*. 83%, 90%, 90% and 21% of that of pristine H-ZSM-5(23), respectively (Scheme 1). This partial recovery of the characteristics of H-ZSM-5 results in a decreased catalyst performance for GTA over Cat-R1. With the increase of reaction - regeneration cycles, the microporosity and Brønsted acidity are further reduced (Scheme 1) due to extended dealumination, leading to more pronounced

irreversible catalyst deactivation after each reaction - regeneration cycle. This study clearly shows the occurrence of reversible and irreversible deactivation after reaction/regeneration cycles. We are currently investigating the mechanism of the deactivation process in more detail, for instance by determination of relevant catalyst properties as a function of the position in the catalyst bed and time on stream.

A possible (partial) solution to reduce H-ZSM-5 framework damage is a reduction in the regeneration temperature (*ca*. 615 °C, DTGA, Figure S7). However, the regeneration time need to be extended in this case to quantitatively remove all coke (*e.g.*, 12 h at 700 °C *versus* 20 h at 615 °C, which was confirmed by several regeneration trails carried out at 615 °C for 12 h, 16 h and 20 h). The trade-off between the time and temperature for regeneration and the effect on the stability of the catalyst should be considered further to develop an improved regeneration procedure. Nevertheless, most of the dealumination and Brønsted acidity loss occur during the first reaction in the sequence using Cat-F. Thus, the development of strategies to enhance the hydrothermal stability of the H-ZSM-5 zeolite under GTA reaction conditions is required.

Irreversible catalyst deactivation was also observed for an H-ZSM-5/bentonite catalyst used for the conversion of crude glycerol [16] as well as for a Sn-H-ZSM-5 when using a glycerol/methanol (40/60 wt.%) feed [10]. When considering the reduction in peak BTX yield after three reaction-regeneration cycles, the un-modified H-ZSM-5 zeolite in this study shows a higher irreversible deactivation level (34%) than Sn-H-ZSM-5 (28%, [10]) and the H-ZSM-5/bentonite catalyst (5%, [16]). This is most likely related to differences in the hydrogen to carbon effective ratio (H/C_{eff}) of the feeds (0.67 for pure glycerol, 1.45 for glycerol/methanol (40/60 wt.%) and *ca*. 1.3 for crude glycerol). It is generally accepted that feeds with a lower H/C_{eff} value show a higher deactivation tendency [17]. The low value for irreversible deactivation for the H-ZSM-5/bentonite catalyst may also be related to binder effects. Therefore, potential solutions to reduce irreversible deactivation of GTA catalysts are the use of co-feeds with a higher H/C_{eff} and the use of H-ZSM-5 in combination with a proper binder. These studies using pure glycerol are currently in progress and will be reported in due course.

The catalytic conversion of glycerol to aromatics *via* an *ex-situ* catalytic pyrolysis approach involves the initial (partial) thermal conversion of glycerol to various intermediates (normally oxygenates, Section 3.1) in a pyrolysis reactor (Figure 1) followed by upgrading of the pyrolysis vapor into aromatics (*e.g.*, BTX) in a dedicated catalytic upgrading reactor (Figure 1). We have

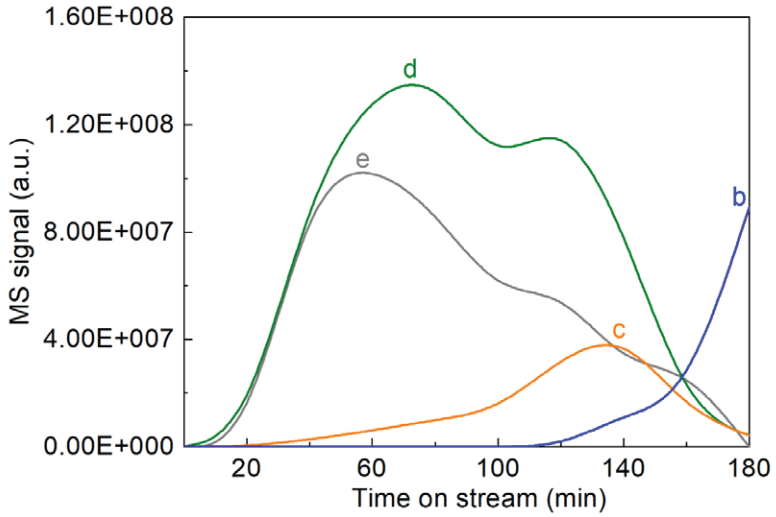

Figure 9. Amount of representative compounds versus runtime (representative components: acetaldehyde for Group b, indane for Group c, benzene for Group d, and naphthalene for Group e) *versus* TOS. The GC-MS peak areas of other compounds are shown in Figure S14.

traced 33 major compounds in the 9 liquid samples (Figure S3) collected every 20 min, which were qualified and semi-quantified by GC-MS (Figure S13) and quantified by GC-FID (Figure S5). The GC-MS peak areas of the individual compounds *versus* TOS are shown in Figure S14. All compounds were lumped into four groups, namely i) oxygenates (Group b, Figure S14 (1 - 6)), ii) bicyclic monoaromatics (BCMAS, Group c, Figure S14 (7 - 9)), iii) BTX (Group d, Figure S14 (10 - 11)) and iv) polycyclic aromatic hydrocarbons (PAHs, *e.g.*, naphthalene, substituted naphthalenes, Group e, Figure S14 (12)). Unconverted glycerol (Group a) was present in the samples when the catalyst activity for aromatics decreased, indicating that glycerol is not fully converted to oxygenates by thermal pyrolysis. This is also confirmed by the data obtained from the non-catalytic pyrolysis of glycerol (Section 3.1). The amounts of the representative compounds for the four lumped groups (*viz*., acetaldehyde for Group b, indane for Group c, benzene for Group d, and naphthalene for Group e) *versus* runtime are shown in Figure 9. Three regimes are visible, start-up of the continuous set-up, a semi-stable phase and a phase in which amounts of aromatics decreases in time due to catalyst deactivation. As expected, in the latter phase, considerable amounts of oxygenates are present in the samples. Major

oxygenates are acrolein, acetaldehyde and acetol, accounting for *ca*. 50% of the total peak area, in line with literature data [29]. Others are 3-hydroxpropanal, formaldehyde, and acetic acid, *etc*. These oxygenates appear in a later stage and increase with TOS (Figure S14). Of interest is the observation that the main type and number of oxygenated compounds formed over the deactivated H-ZSM-5 catalyst (Figure S14 and Scheme S1) are different from those formed by non-catalytic pyrolysis (Section 3.1). This indicates that the deactivated H-ZSM-5 catalyst, though not active for aromatics formation, still catalyzes the conversions of glycerol/intermediates to other oxygenates.

The data presented in this study, show that the three groups of aromatics (Groups c, d and e, Figure 9) likely form simultaneously. However, the BCMAS (Group c) seem to be completely converted to BTX (Group d) and PAHS (Group e), evidenced by the negligible formation in the initial stage of reaction (*e.g*., TOS < 60 min), in line with data by Heeres *et al* [50]. The amount of BTX (group c) shows the typical volcano type trend, with a short period (*e.g*., TOS of 80 -120 min) of stable BTX production stage. However, the yields of benzene and toluene decrease and xylenes yield increase with an increase of TOS from 80 min to 120 min. A reaction pathway for GTA *via* an *ex-situ* catalytic pyrolysis approach is proposed in Scheme S1, neglecting the gaseous products (*e.g*., CO, CO_2, H_2 and C_1 - C_3 hydrocarbons). Glycerol is first transformed to C1 (*e.g*., formaldehyde), C2 (*e.g*., acetaldehyde) and C3 oxygenates (*e.g*., acrolein) *via* deoxygenation and thermal cracking under pyrolysis conditions (Section 3.1). These reactive oxygenates may be converted to higher molecular weight compounds, ultimately leading to char/coke formation, or converted to aromatics (BTX, BCMAS and PAHS) *via* deoxygenation and aromatization reactions catalyzed by the H-ZSM-5 zeolite. The bicyclic monoaromatics (BCMAS) may be converted to BTX and PAHS *via* dehydrogenation, dealkylation and disproportionation over the very active acidic sites of H-ZSM-5 catalyst. The substituted aromatics can also be converted to aromatics *via* dealkylation. Besides, some of the aromatics in Groups c, d and e may also be coke precursors, leading to coke formation on the catalyst.

4. Conclusions

The catalytic conversion of glycerol to aromatics *via* an *ex-situ* catalytic pyrolysis approach using pure glycerol as the feed and an unmodified H-ZSM-5(23) zeolite as the catalyst has been investigated in a continuous unit. This combination of feed, catalyst and approach has

to the best of our knowledge not been investigated in the literature and is an absolute novelty of this work. At the prevailing reaction conditions, the peak BTX yield was 28.1 ± 0.2% on carbon basis (12.1 ± 0.1 wt.% on weight basis), which is considerably higher than the literature values for an unmodified H-ZSM-5 catalyst. Catalyst deactivation was shown to occur on a timescale of hours due to coke formation. Furthermore, the selectivity of the individual BTX components is a function of the TOS, with longer times on stream leading to higher amounts of xylenes. It was shown that the deactivated catalyst can *in-situ* be regenerated by an oxidative treatment at 700 °C. Four regeneration-reaction cycles were performed, showing *ca*. 15% BTX productivity loss after each cycle, indicating some irreversible catalyst deactivation. Extensive catalyst characterization studies show that irreversible deactivation is due to dealumination of the H-ZSM-5(23) framework, leading to a slightly reduced micro-porosity and remarkably loss of Brønsted acid sites. It is also shown that deactivation mainly occurs during the actual *ex-situ* catalytic pyrolysis of glycerol, likely due to water formation. The latter was shown to be formed mainly in the catalytic upgrading reactor, and at a lesser extent during glycerol pyrolysis.

As such, this study has provided new insights in the mechanisms for catalyst deactivation and its consequences on BTX yields and selectivity for the conversion of glycerol to bio-based chemicals over zeolite based catalysts. It indicates that proper modification of the H-ZSM-5 zeolite catalyst will be required to improve performance, and particularly to reduce irreversible catalyst deactivation by dealumination. Possible solutions are the use of binders in the catalyst formulation (*e.g*. Al_2O_3 and clays), and a reduction of the hydrophilicity of the H-ZSM-5 catalyst. These studies are in progress and will be reported in due course. In addition, this study also provides relevant information for the scale up of the GTA technology. The deactivation rate of the catalyst, both reversible and irreversible ones are of high relevance for the design of the regeneration unit and to determine the catalyst usage (addition of fresh catalyst to maintain activity due to irreversible deactivation). The latter is a major cost item for the GTA process and will significantly affect the techno-economic viability.

Supporting information

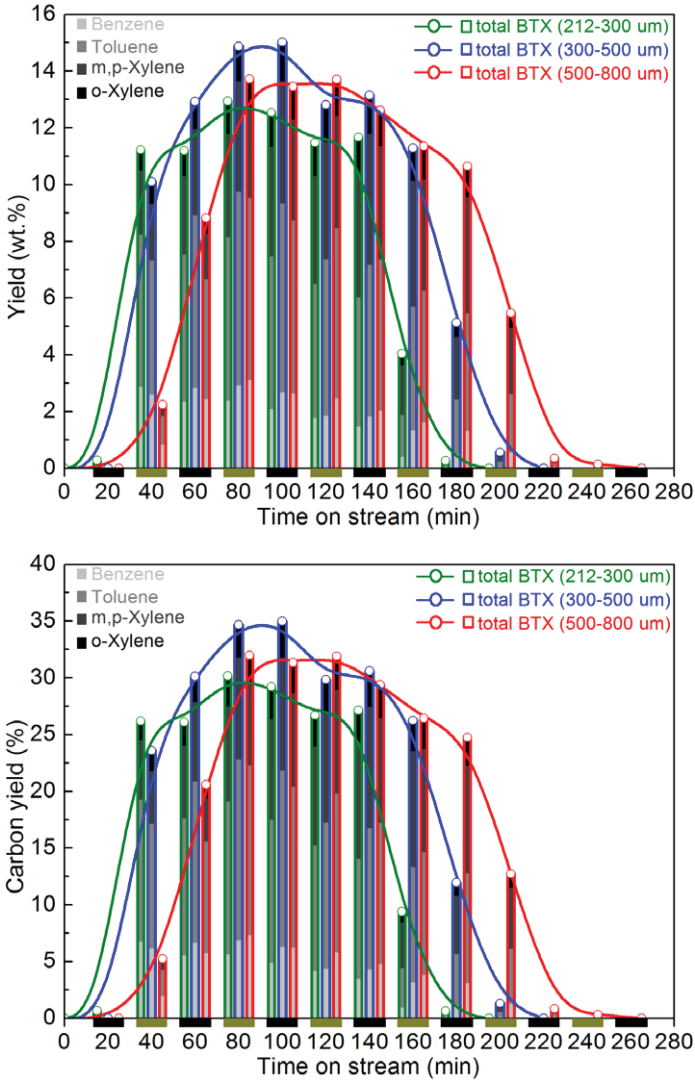

Figure S1. Yields of BTX *versus* TOS with different catalyst particle size. Reaction conditions are: pyrolysis temperature and catalytic upgrading temperature were 500 °C, atmospheric pressure, N_2 flow was 1.8 ml min^{-1}, loading of H-ZSM-5(23) zeolite was 1 g, and WHSV of glycerol was 1 h^{-1}.

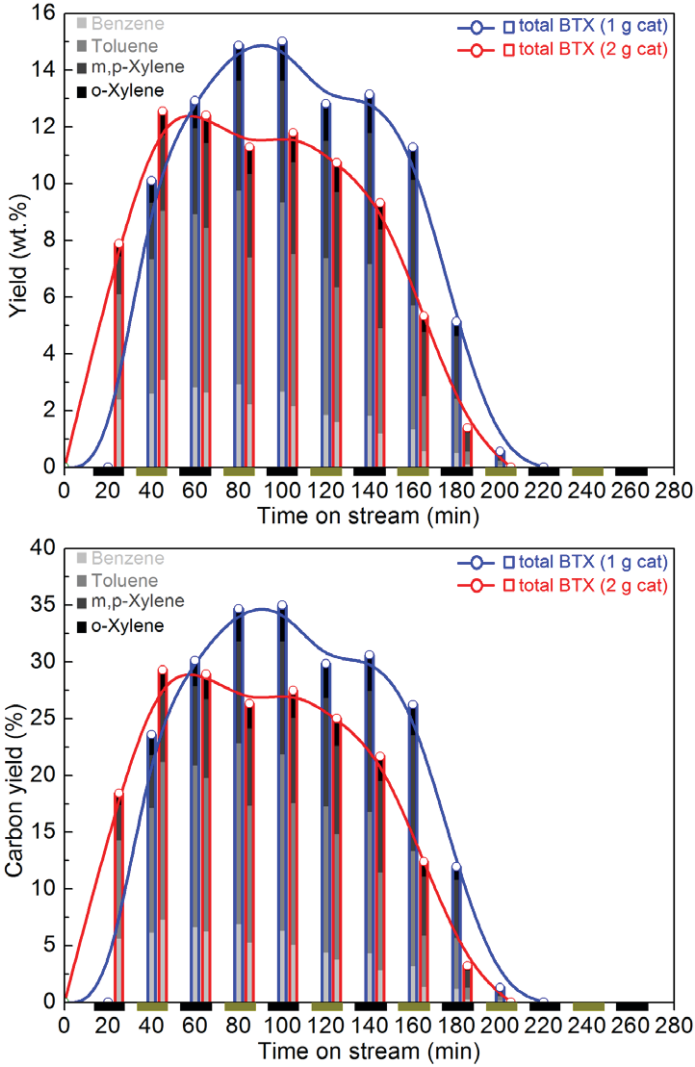

Figure S2. Yields of BTX *versus* TOS with different catalyst loading. Reaction conditions are: pyrolysis temperature and catalytic upgrading temperature were 500 °C, atmospheric pressure, N_2 flow was 1.8 ml min^{-1} (for 1 g catalyst loading) and 3.6 ml min^{-1} (for 2 g catalyst loading), H-ZSM-5(23) particle size was 300 - 500 µm, and WHSV of glycerol was 1 h^{-1}.

Figure S3. Representative products collected in the 4-ml sample vials at different TOS. Reaction conditions are: pyrolysis temperature was 487 °C, catalytic upgrading temperature was 500 °C, atmospheric pressure, N_2 flow was 1.8 ml min^{-1}, H-ZSM-5(23) particle size was 500 - 800 µm, and glycerol feed was 1 g h^{-1}.

Figure S4. The overall biphasic liquid products collected in the 20-ml sample vial from the experiment to check the mass balance, carbon balance and oxygen balance. Reaction conditions are: pyrolysis temperature was 400 °C, catalytic upgrading temperature was 500 °C, atmospheric pressure, N_2 flow was 1.8 ml min^{-1}, H-ZSM-5(23) particle size was 300 - 500 µm, glycerol feed was 1 g h^{-1}, and TOS was 5 h.

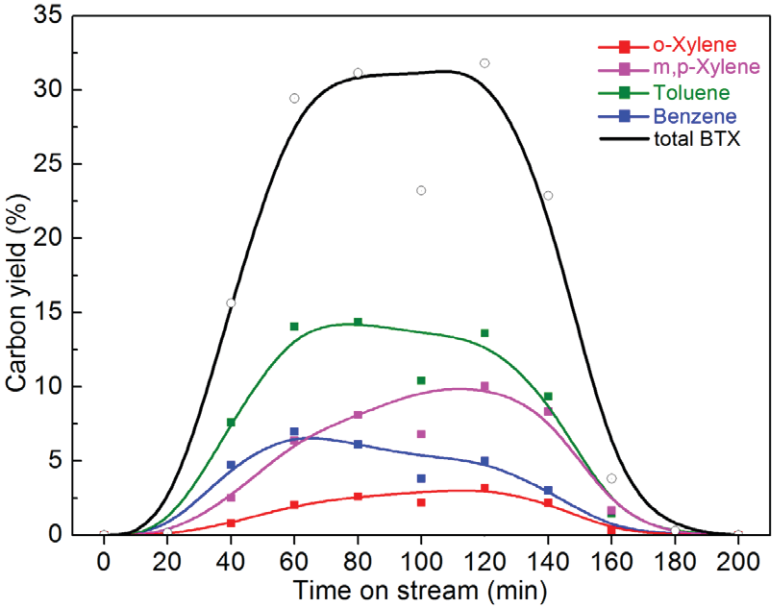

Figure S5. Yields of BTX *versus* TOS. Reaction conditions are: pyrolysis temperature was 487 °C, catalytic upgrading temperature was 500 °C, atmospheric pressure, N_2 flow was 1.8 ml min^{-1}, H-ZSM-5(23) particle size was 500 - 800 µm, and glycerol feed was 1 g h^{-1}.

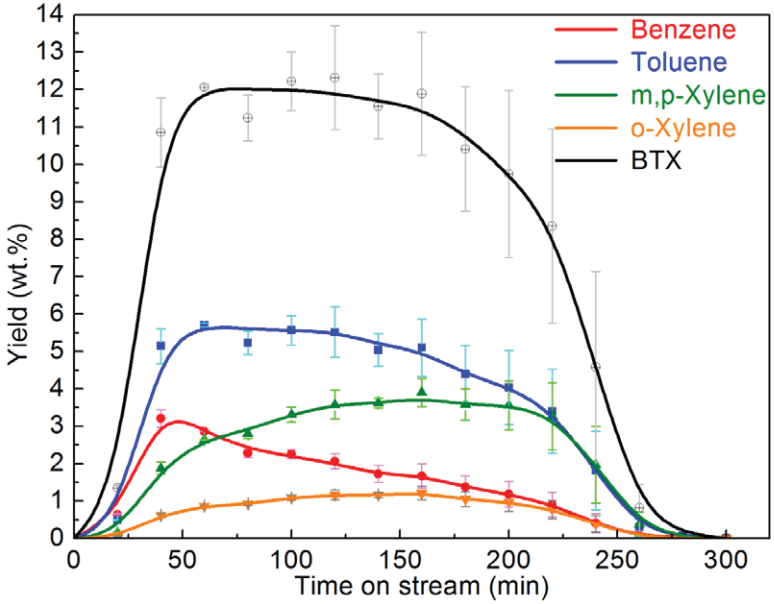

Figure S6. Yield of the individual BTX *versus* TOS. Reaction conditions are: pyrolysis temperature was 400 °C, catalytic upgrading temperature was 500 °C, atmospheric pressure, N_2 flow was 1.8 ml min^{-1}, H-ZSM-5(23) particle size was 300 - 500 µm, loading of H-ZSM-5(23) zeolite was 1 g, and WHSV of glycerol was 1 h^{-1}.

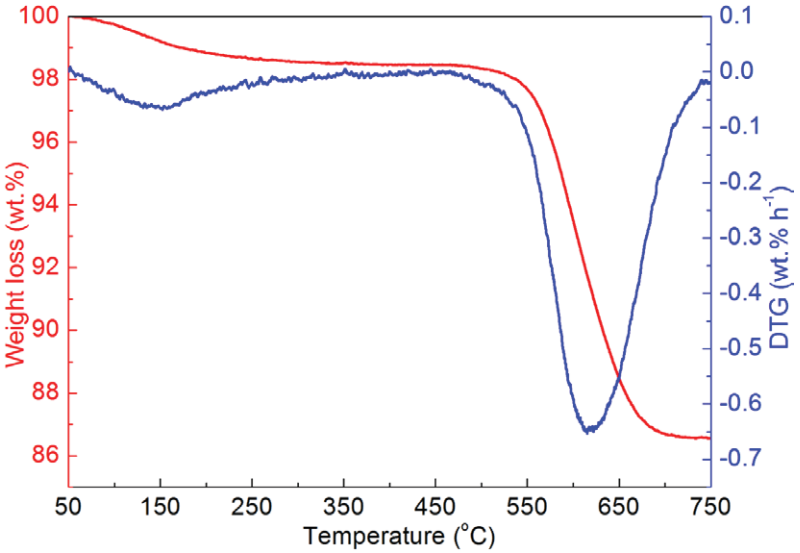

Figure S7. TG-DTG curves of the deactivated H-ZSM-5(23) catalyst. Reaction conditions are: pyrolysis temperature was 400 °C, catalytic upgrading temperature was 500 °C, atmospheric pressure, N_2 flow was 1.8 ml min^{-1}, H-ZSM-5(23) particle size was 300 - 500 µm, loading of H-ZSM-5(23) zeolite was 1 g, and WHSV of glycerol was 1 h^{-1}.

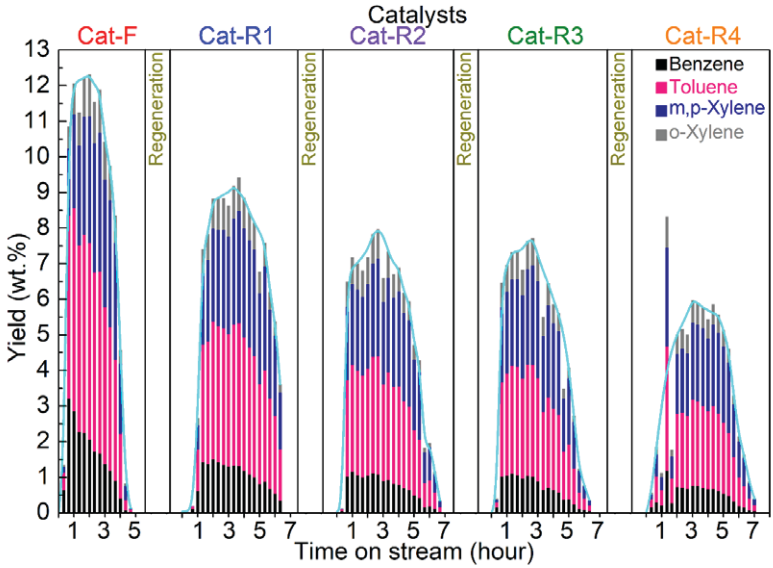

Figure S8. Yields of BTX over the fresh and regenerated H-ZSM-5(23) catalysts *versus* TOS. Reaction conditions are: pyrolysis temperature was 400 °C, catalytic upgrading temperature was 500 °C, atmospheric pressure, N_2 flow was 1.8 ml min^{-1}, H-ZSM-5(23) particle size was 300 - 500 µm, loading of H-ZSM-5(23) zeolite was 1 g, and WHSV of glycerol was 1 h^{-1}.

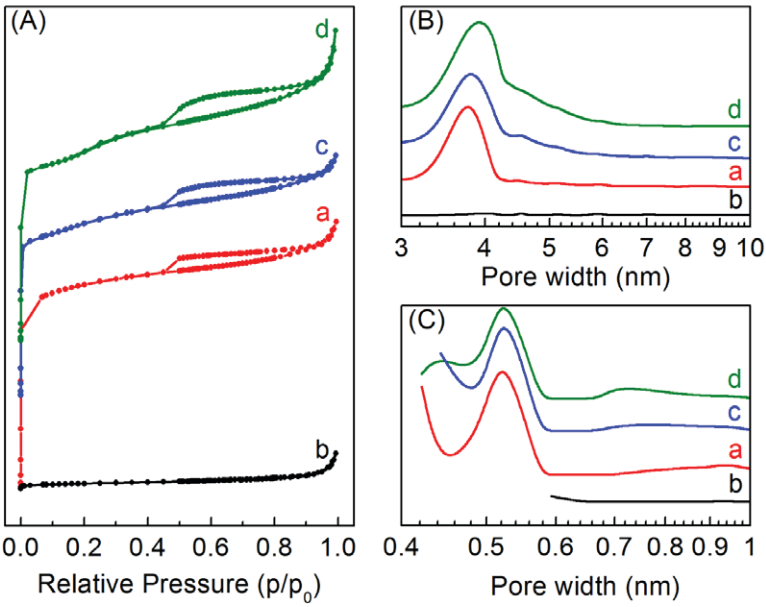

Figure S9. N_2 adsorption-desorption isotherms (A), BJH meso-pore size distribution (B) and NLDFT micro-pore size distribution (C) of (a) Cat-F, (b) Cat-D, (c) Cat-R1, and (d) Cat-R5.

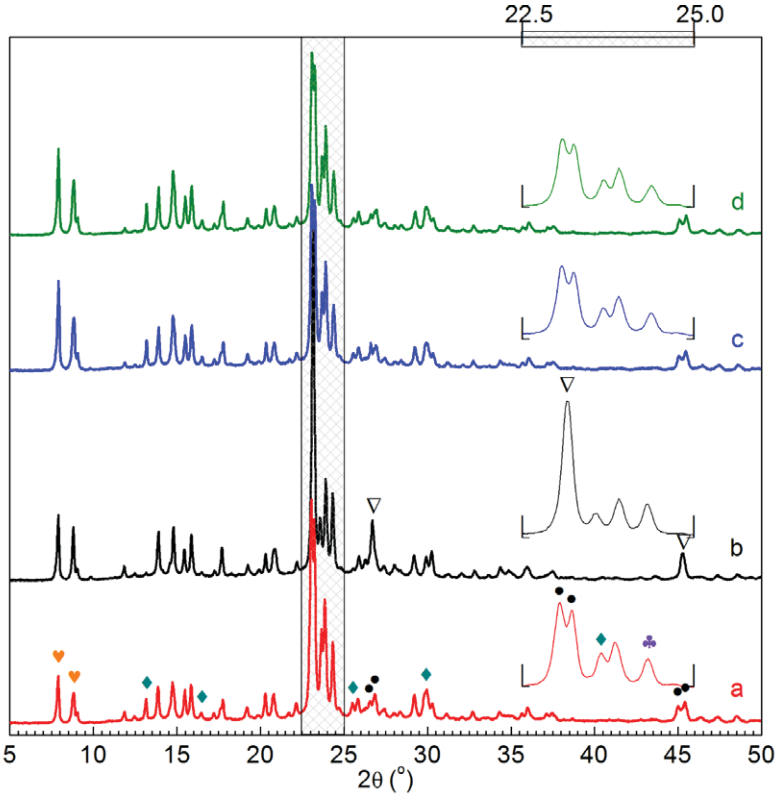

Figure S10. XRD patterns of (a) Cat-F, (b) Cat-D, (c) Cat-R1, and (d) Cat-R5.

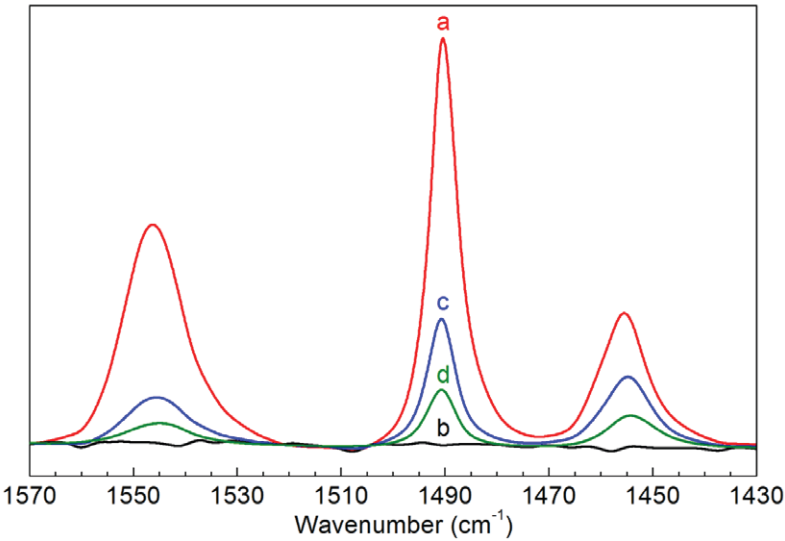

Figure S11. Pyridine-IR spectra of (a) Cat-F, (b) Cat-D, (c) Cat-R1, and (d) Cat-R5.

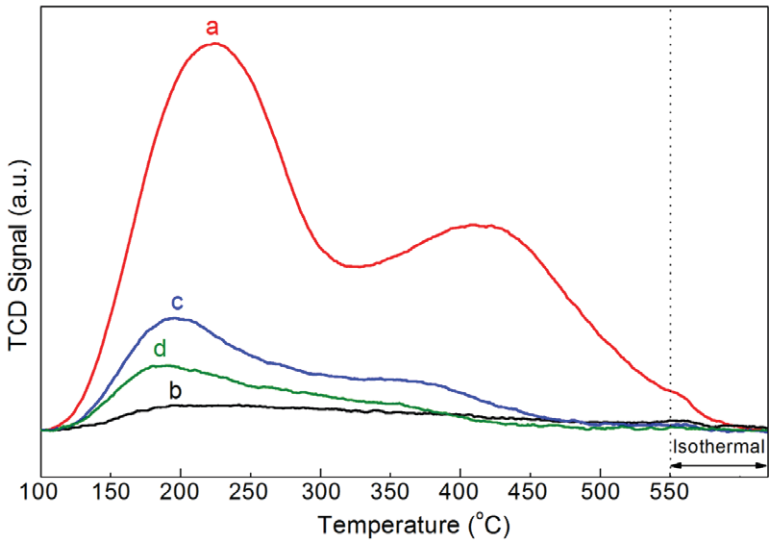

Figure S12. NH_3-TPD profiles of (a) Cat-F, (b) Cat-D, (c) Cat-R1, and (d) Cat-R5.

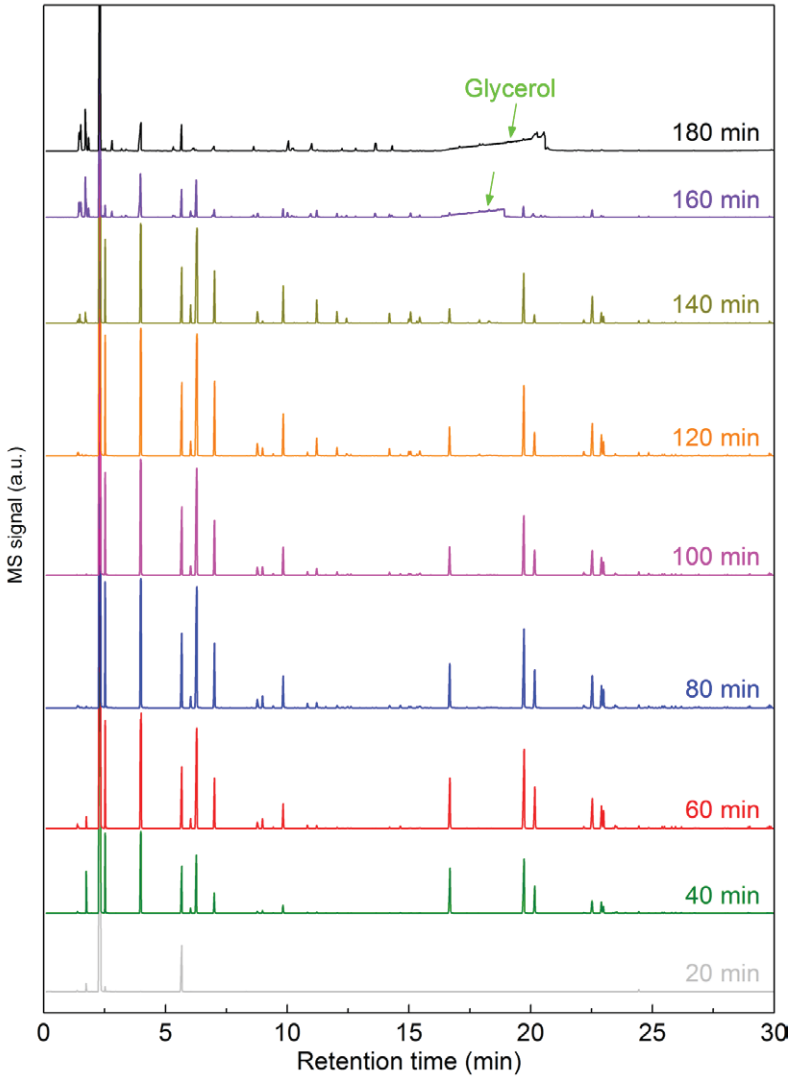

Figure S13. GC-MS chromatograph of the liquid products collected at different TOS. Reaction conditions are: pyrolysis temperature was 487 °C, catalytic upgrading temperature was 500 °C, atmospheric pressure, N_2 flow was 1.8 ml min^{-1}, H-ZSM-5(23) particle size was 500 - 800 µm, and glycerol feed was 1 g h^{-1}.

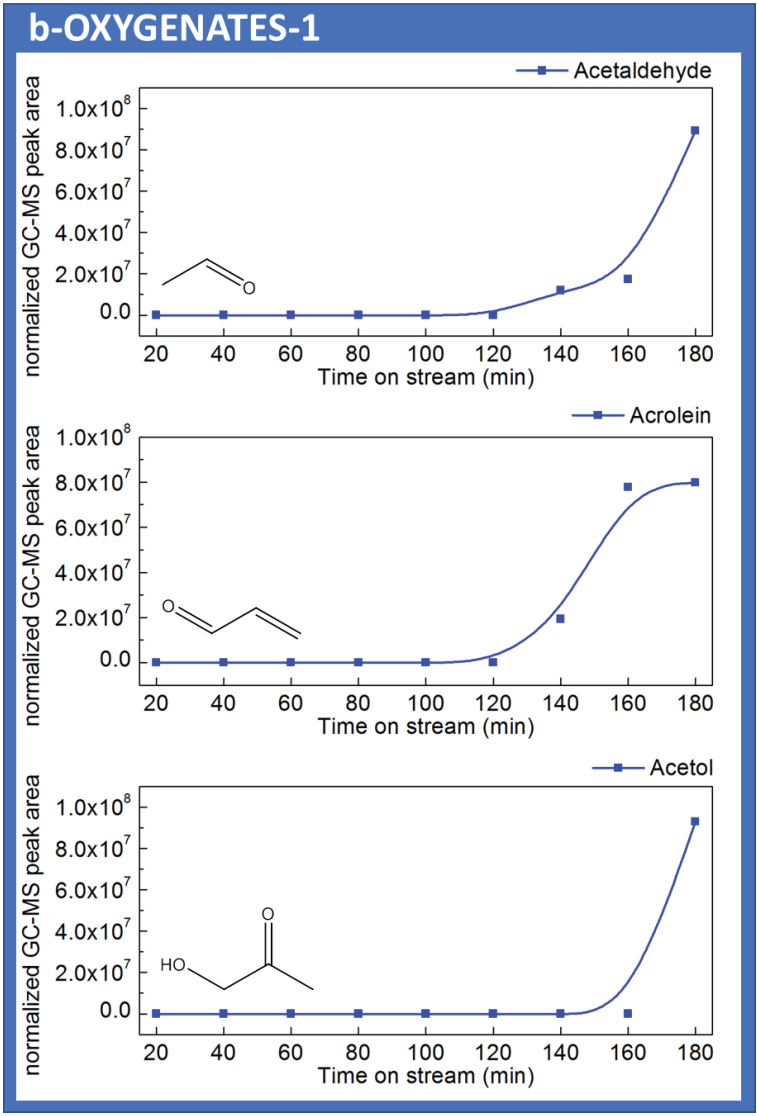

Figure S14-1. Normalized GC-MS peak area of the individual product *versus* TOS. Reaction conditions are: pyrolysis temperature was 487 °C, catalytic upgrading temperature was 500 °C, atmospheric pressure, N_2 flow was 1.8 ml min^{-1}, H-ZSM-5(23) particle size was 500 - 800 µm, and glycerol feed was 1 g h^{-1}.

(*Continued from the previous page*)

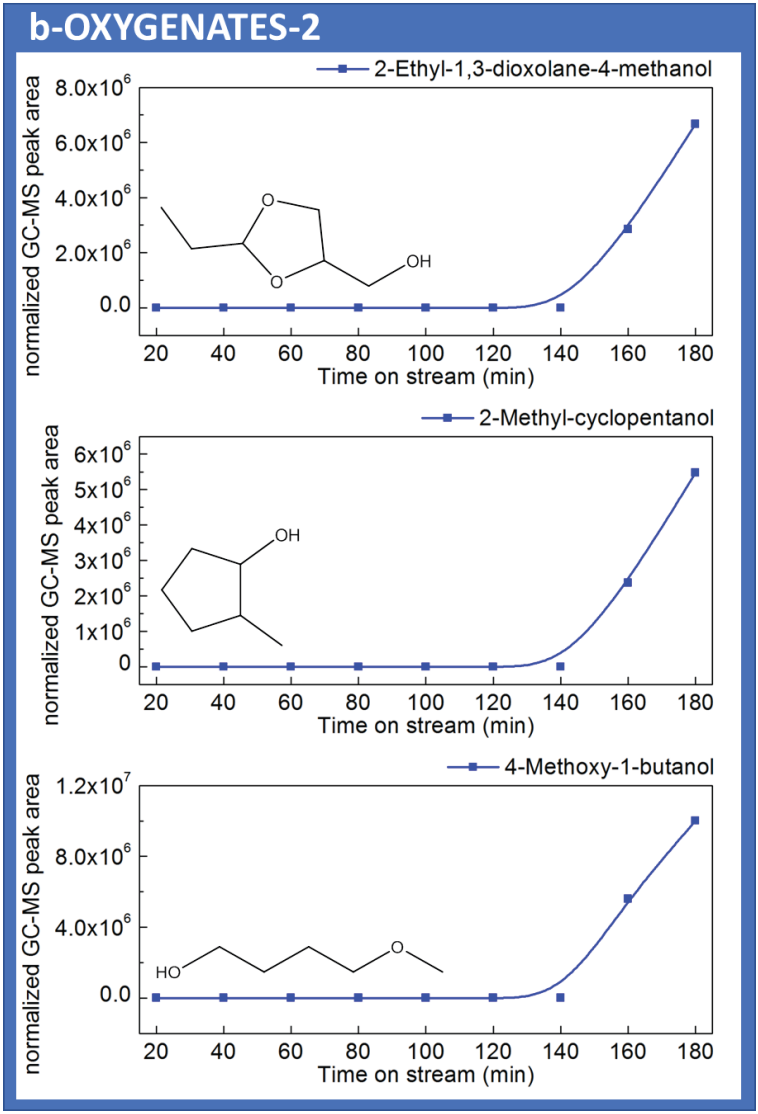

Figure S14-2. Normalized GC-MS peak area of the individual product *versus* TOS. Reaction conditions are: pyrolysis temperature was 487 °C, catalytic upgrading temperature was 500 °C, atmospheric pressure, N_2 flow was 1.8 ml min^{-1}, H-ZSM-5(23) particle size was 500 - 800 µm, and glycerol feed was 1 g h^{-1}.

(*Continued from the previous page*)

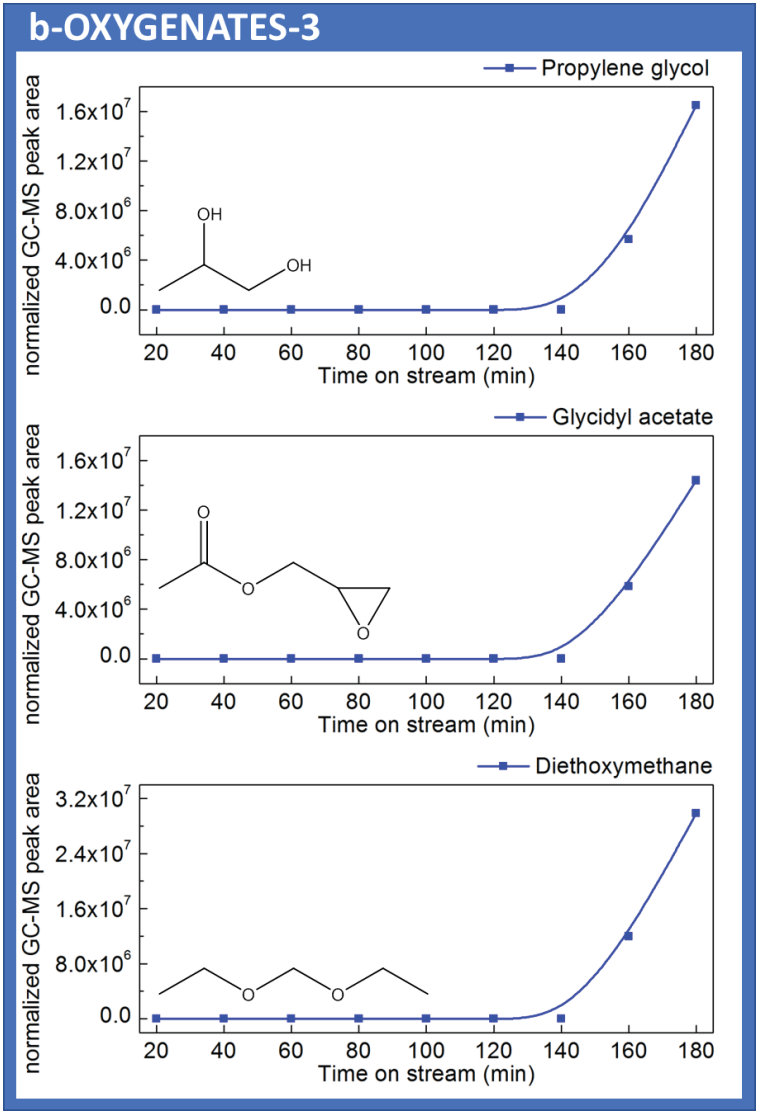

Figure S14-3. Normalized GC-MS peak area of the individual product *versus* TOS. Reaction conditions are: pyrolysis temperature was 487 °C, catalytic upgrading temperature was 500 °C, atmospheric pressure, N_2 flow was 1.8 ml min^{-1}, H-ZSM-5(23) particle size was 500 - 800 µm, and glycerol feed was 1 g h^{-1}.

(*Continued from the previous page*)

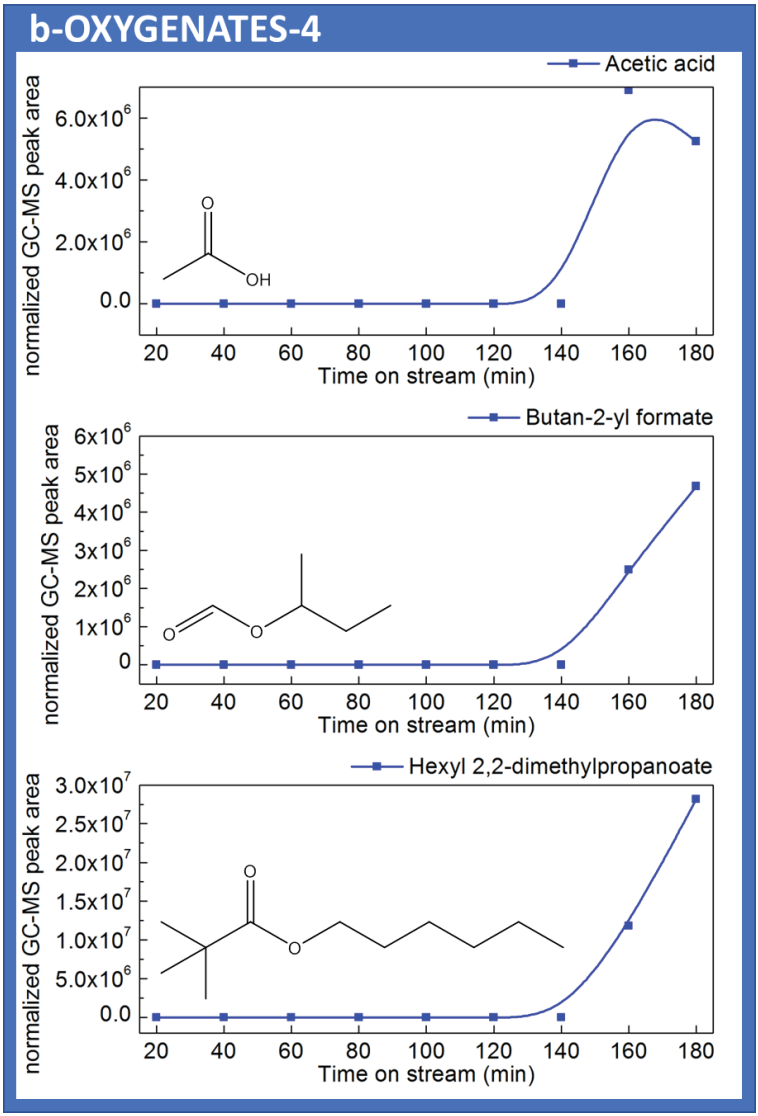

Figure S14-4. Normalized GC-MS peak area of the individual product *versus* TOS. Reaction conditions are: pyrolysis temperature was 487 °C, catalytic upgrading temperature was 500 °C, atmospheric pressure, N_2 flow was 1.8 ml min^{-1}, H-ZSM-5(23) particle size was 500 - 800 µm, and glycerol feed was 1 g h^{-1}.

(*Continued from the previous page*)

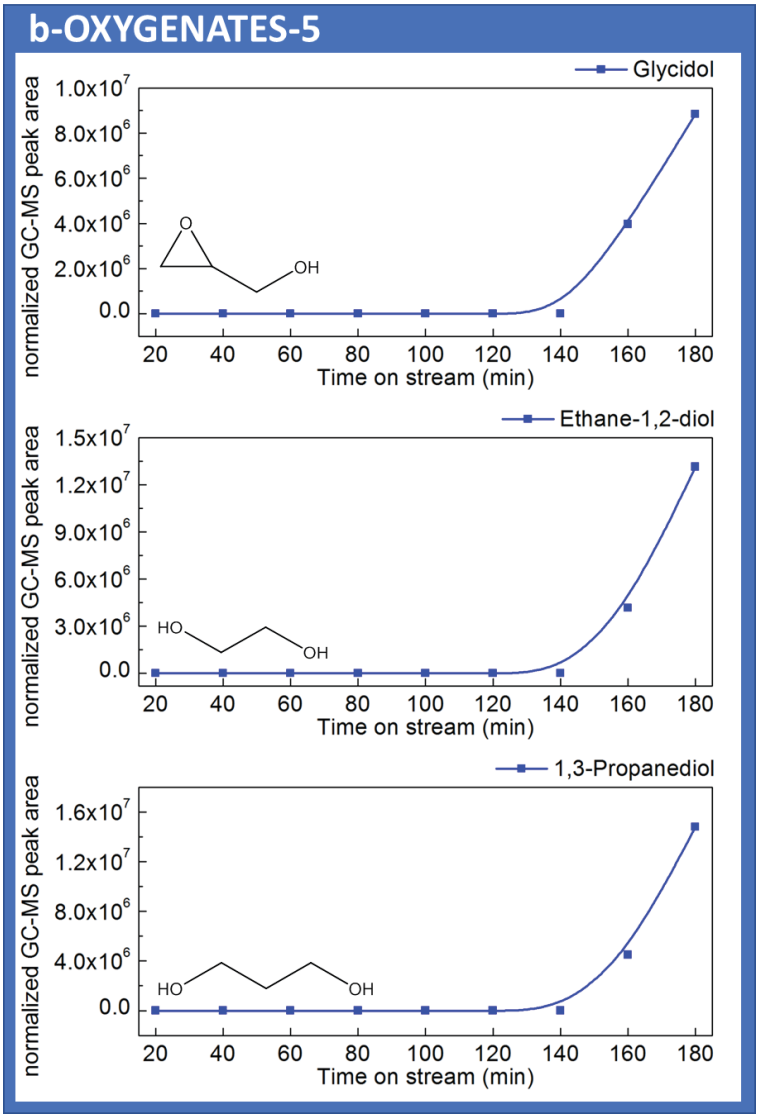

Figure S14-5. Normalized GC-MS peak area of the individual product *versus* TOS. Reaction conditions are: pyrolysis temperature was 487 °C, catalytic upgrading temperature was 500 °C, atmospheric pressure, N_2 flow was 1.8 ml min^{-1}, H-ZSM-5(23) particle size was 500 - 800 µm, and glycerol feed was 1 g h^{-1}.

(*Continued from the previous page*)

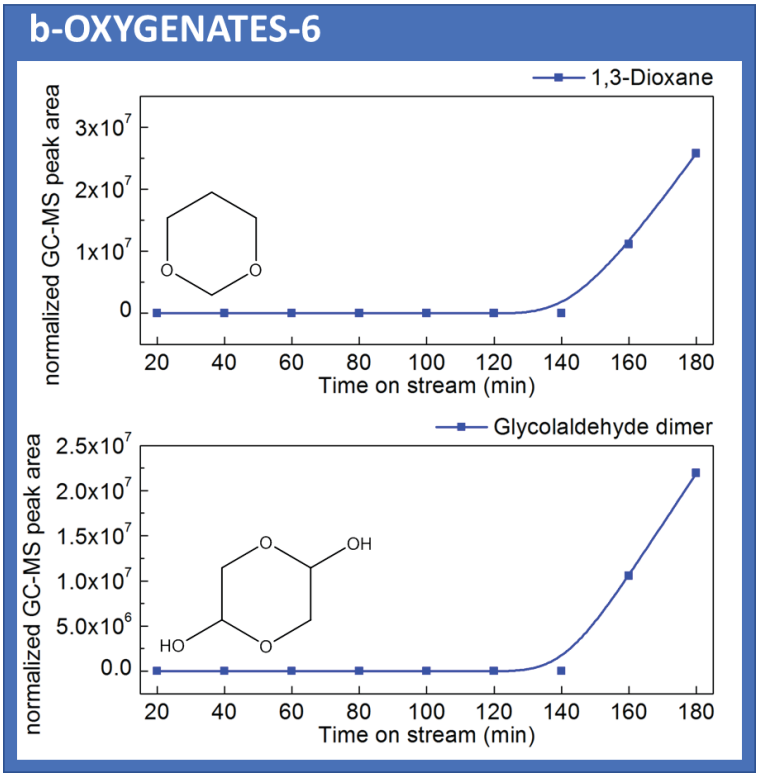

Figure S14-6. Normalized GC-MS peak area of the individual product *versus* TOS. Reaction conditions are: pyrolysis temperature was 487 °C, catalytic upgrading temperature was 500 °C, atmospheric pressure, N_2 flow was 1.8 ml min^{-1}, H-ZSM-5(23) particle size was 500 - 800 µm, and glycerol feed was 1 g h^{-1}.

(*Continued from the previous page*)

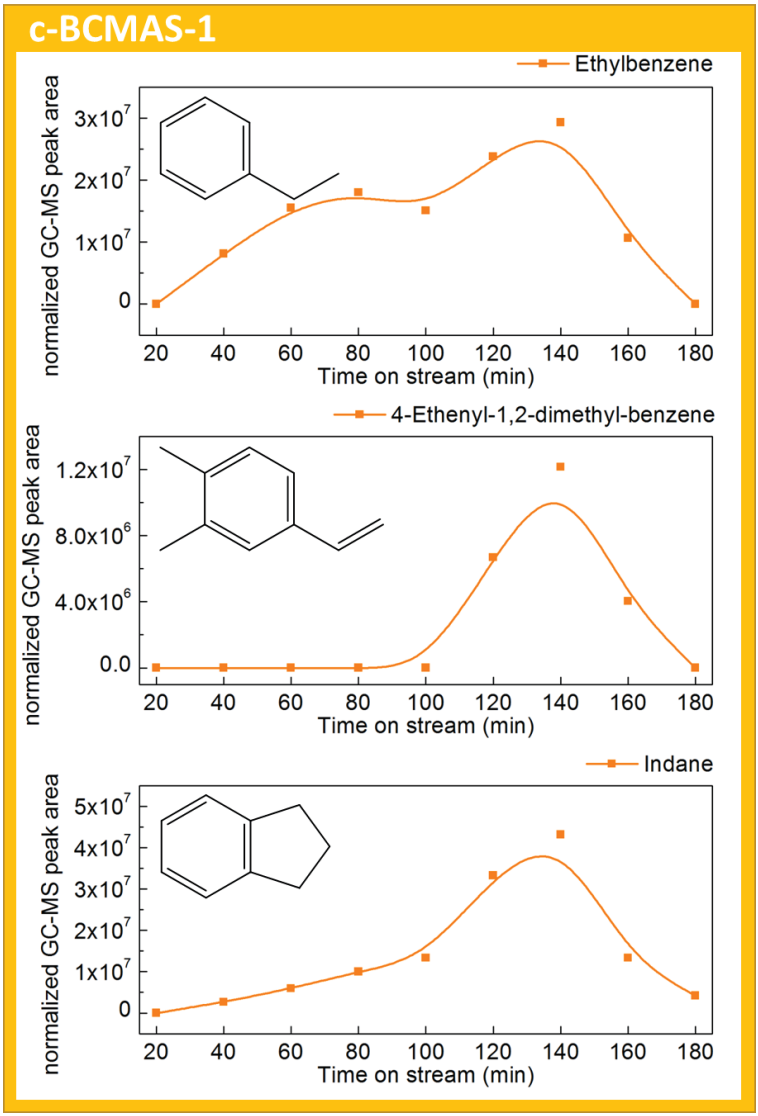

Figure S14-7. Normalized GC-MS peak area of the individual product *versus* TOS. Reaction conditions are: pyrolysis temperature was 487 °C, catalytic upgrading temperature was 500 °C, atmospheric pressure, N_2 flow was 1.8 ml min^{-1}, H-ZSM-5(23) particle size was 500 - 800 µm, and glycerol feed was 1 g h^{-1}.

(*Continued from the previous page*)

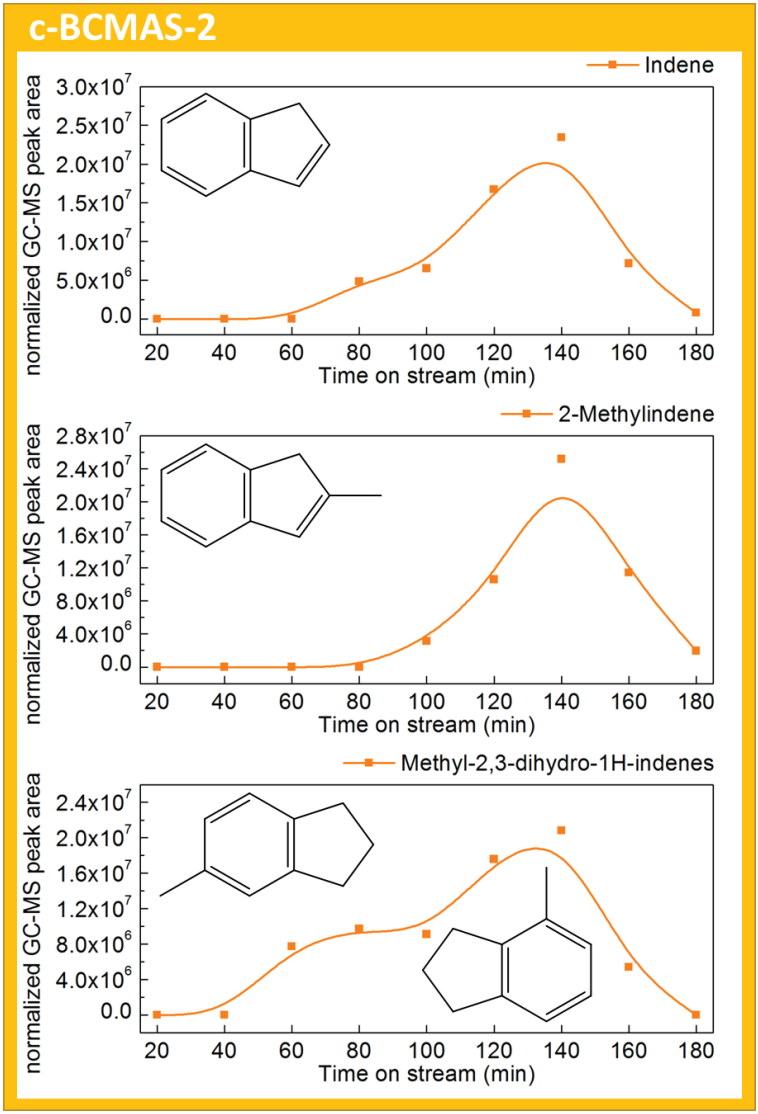

Figure S14-8. Normalized GC-MS peak area of the individual product *versus* TOS. Reaction conditions are: pyrolysis temperature was 487 °C, catalytic upgrading temperature was 500 °C, atmospheric pressure, N_2 flow was 1.8 ml min^{-1}, H-ZSM-5(23) particle size was 500 - 800 µm, and glycerol feed was 1 g h^{-1}.

(*Continued from the previous page*)

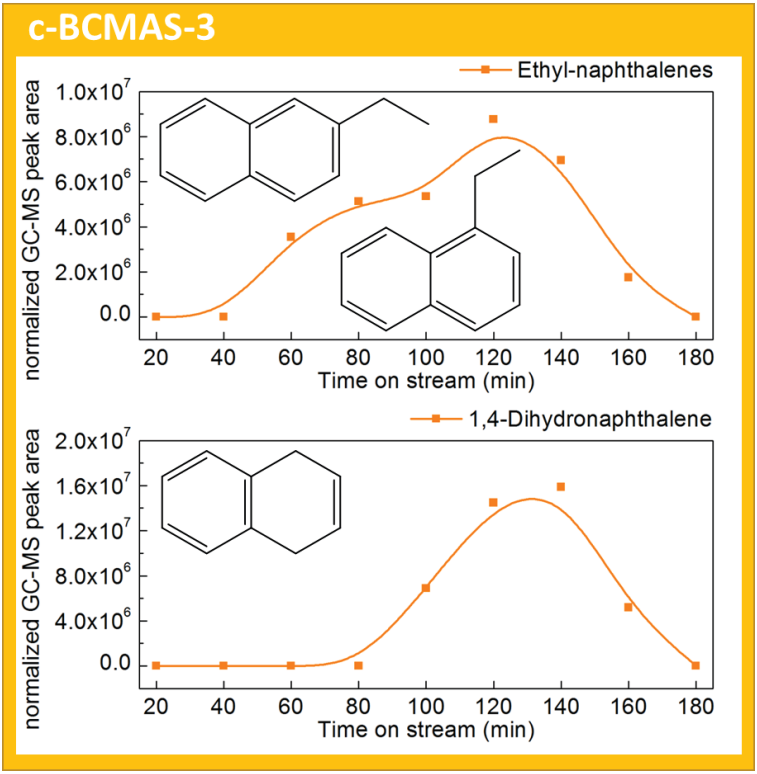

Figure S14-9. Normalized GC-MS peak area of the individual product *versus* TOS. Reaction conditions are: pyrolysis temperature was 487 °C, catalytic upgrading temperature was 500 °C, atmospheric pressure, N_2 flow was 1.8 ml min^{-1}, H-ZSM-5(23) particle size was 500 - 800 µm, and glycerol feed was 1 g h^{-1}.

(*Continued from the previous page*)

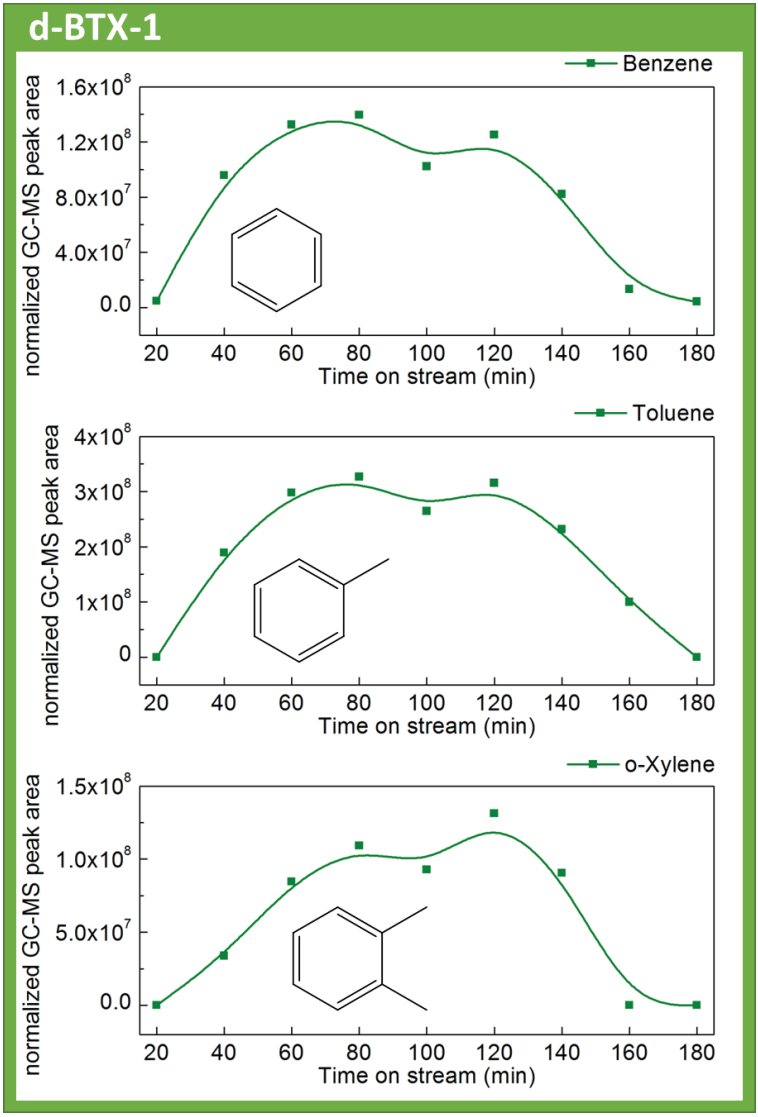

Figure S14-10. Normalized GC-MS peak area of the individual product *versus* TOS. Reaction conditions are: pyrolysis temperature was 487 °C, catalytic upgrading temperature was 500 °C, atmospheric pressure, N_2 flow was 1.8 ml min^{-1}, H-ZSM-5(23) particle size was 500 - 800 µm, and glycerol feed was 1 g h^{-1}.

(*Continued from the previous page*)

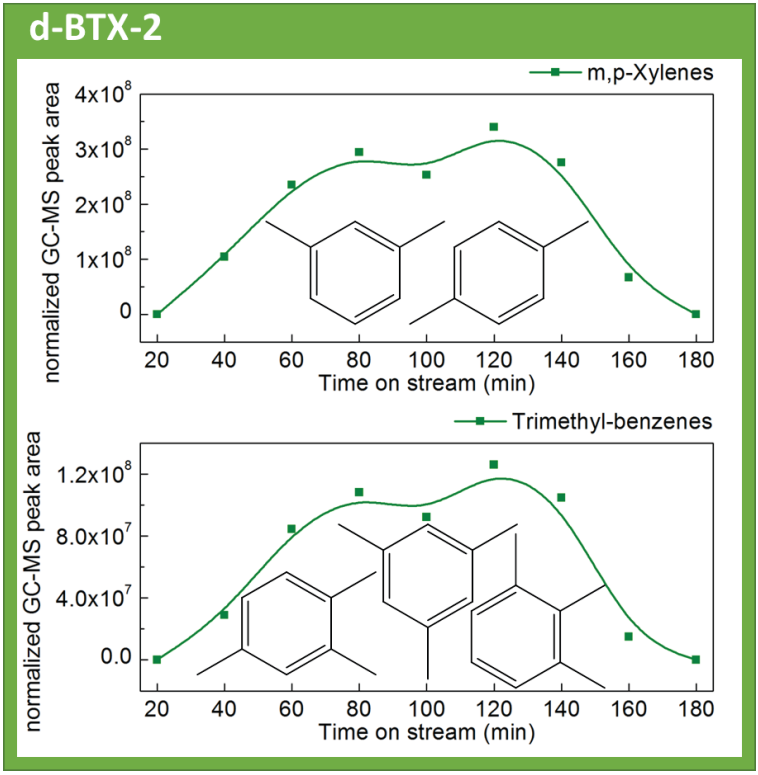

Figure S14-11. Normalized GC-MS peak area of the individual product *versus* TOS. Reaction conditions are: pyrolysis temperature was 487 °C, catalytic upgrading temperature was 500 °C, atmospheric pressure, N_2 flow was 1.8 ml min^{-1}, H-ZSM-5(23) particle size was 500 - 800 µm, and glycerol feed was 1 g h^{-1}.

(*Continued from the previous page*)

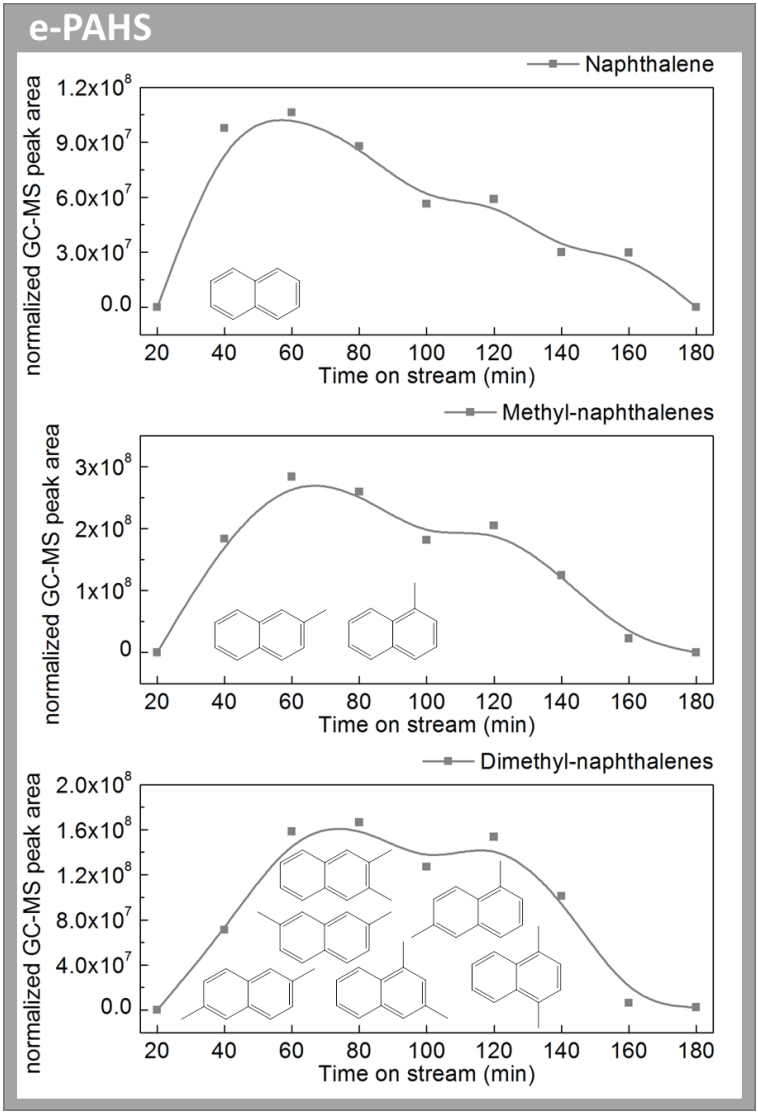

Figure S14-12. Normalized GC-MS peak area of the individual product *versus* TOS. Reaction conditions are: pyrolysis temperature was 487 °C, catalytic upgrading temperature was 500 °C, atmospheric pressure, N_2 flow was 1.8 ml min^{-1}, H-ZSM-5(23) particle size was 500 - 800 µm, and glycerol feed was 1 g h^{-1}.

References

[1] C.M. Lok, J. Van Doorn, G.A. Almansa, Promoted ZSM-5 catalysts for the production of bio-aromatics, a review, Renew. Sust. Energ. Rev. 113 (2019) Article 109248.
[2] M. Ayoub, A.Z. Abdullah, Critical review on the current scenario and significance of crude glycerol resulting from biodiesel industry towards more sustainable renewable energy industry, Renew. Sust. Energ. Rev. 16 (2012) 2671-2686.
[3] O. Muraza, Peculiarities of glycerol conversion to chemicals over zeolite-based catalysts, Front. Chem. 7 (2019) Article 233.
[4] M.R. Monteiro, C.L. Kugelmeier, R.S. Pinheiro, M.O. Batalha, A. da Silva César, Glycerol from biodiesel production: Technological paths for sustainability, Renew. Sust. Energ. Rev. 88 (2018) 109-122.
[5] L.C. Meher, D.V. Sagar, S.N. Naik, Technical aspects of biodiesel production by transesterification - a review, Renew. Sust. Energ. Rev. 10 (2006) 248-268.
[6] C.H.C. Zhou, J.N. Beltramini, Y.X. Fan, G.Q.M. Lu, Chemoselective catalytic conversion of glycerol as a biorenewable source to valuable commodity chemicals, Chem. Soc. Rev. 37 (2008) 527-549.
[7] T.Q. Hoang, X.L. Zhu, T. Danuthai, L.L. Lobban, D.E. Resasco, R.G. Mallinson, Conversion of glycerol to alkyl-aromatics over zeolites, Energy Fuels 24 (2010) 3804-3809.
[8] Y.-W. Suh, H.-S. Jang, K.-B. Bae Method for producing bio-aromatics from glycerol. US2015336856A1, 20151126, 2015.
[9] S. Tamiyakul, W. Ubolcharoen, D.N. Tungasmita, S. Jongpatiwut, Conversion of glycerol to aromatic hydrocarbons over Zn-promoted HZSM-5 catalysts, Catal. Today 256 (2015) 325-335.
[10] F. Wang, W.Y. Xiao, L.J. Gao, G.M. Xiao, Enhanced performance of glycerol to aromatics over Sn-containing HZSM-5 zeolites, RSC Adv. 6 (2016) 42984-42993.
[11] Y. Xiao, A. Varma, Conversion of glycerol to hydrocarbon fuels *via* bifunctional catalysts, ACS Energy Lett. 1 (2016) 963-968.
[12] F. Wang, X.Z. Chu, F.X. Zhu, F.Y. Wu, Q.Q. Li, B.H. Liu, G.M. Xiao, Producing BTX aromatics-enriched oil from biomass derived glycerol using dealuminated HZSM-5 by successive steaming and acid leaching as catalyst: Reactivity, acidity and product distribution, Microporous Mesoporous Mater. 277 (2019) 286-294.
[13] W.Y. Xiao, F. Wang, G.M. Xiao, Performance of hierarchical HZSM-5 zeolites prepared by NaOH treatments in the aromatization of glycerol, RSC Adv. 5 (2015) 63697-63704.
[14] X.H. Yang, F. Wang, R.P. Wei, S. Li, Y.F. Wu, P.X. Shen, H.Z. Wang, L.J. Gao, G.M. Xiao, Synergy effect between hierarchical structured and Sn-modified H [Sn, Al]ZSM-5 zeolites on the catalysts for glycerol aromatization, Microporous Mesoporous Mater. 257 (2018) 154-161.
[15] L.H. Dao, M. Haniff, A. Houle, D. Lamothe, Reactions of model compounds of biomass-pyrolysis oils over ZSM-5 zeolite catalysts, ACS Symp. Ser. 376 (1988) 328-341.
[16] S. He, I. Muizebelt, A. Heeres, N.J. Schenk, R. Blees, H.J. Heeres, Catalytic pyrolysis of crude glycerol over shaped ZSM-5/bentonite catalysts for bio-BTX synthesis, Appl. Catal., B 235 (2018) 45-55.
[17] H.Y. Zhang, Y.T. Cheng, T.P. Vispute, R. Xiao, G.W. Huber, Catalytic conversion of biomass-derived feedstocks into olefins and aromatics with ZSM-5: the hydrogen to carbon effective ratio, Energy Environ. Sci. 4 (2011) 2297-2307.
[18] H.S. Jang, K. Bae, M. Shin, S.M. Kim, C.U. Kim, Y.W. Suh, Aromatization of glycerol/alcohol mixtures over zeolite H-ZSM-5, Fuel 134 (2014) 439-447.
[19] A.L. Tarasov, Catalytic conversion of glycerol into aromatic hydrocarbons, acrolein, and glycerol ethers on zeolite catalysts, Russ. J. Phys. Chem. A 92 (2018) 2451-2454.

[20] D. Kumar, N. Anand, K.K. Pant, Glycerol conversion over palladium- and alumina-impregnated KIT-6 for the production of gasoline range hydrocarbons, Clean Technol. Environ. Policy 20 (2018) 751-757.
[21] Y.-W. Suh, M. Shin Method for producing bio-aromatic compounds using glycerol. KR1020150073951, 20161207, 2016.
[22] A. Shahnazari, Catalytic co-conversion of glycerol and proton-donor species to gasoline-range aromatics over alumina, The University of New Brunswick, 113, 2016. (accessed on 201609).
[23] A. Errekatxo, A. Ibarra, A. Gutierrez, J. Bilbao, J.M. Arandes, P. Castano, Catalytic deactivation pathways during the cracking of glycerol and glycerol/VGO blends under FCC unit conditions, Chem. Eng. J. 307 (2017) 955-965.
[24] Y. Xiao, A. Varma, Kinetics of glycerol conversion to hydrocarbon fuels over Pd/H-ZSM-5 catalyst, AICHE Journal 63 (2017) 5445-5451.
[25] A. Corma, G.W. Huber, L. Sauvanaud, P. O'Connor, Processing biomass-derived oxygenates in the oil refinery: Catalytic cracking (FCC) reaction pathways and role of catalyst, J. Catal. 247 (2007) 307-327.
[26] J.C. Groen, L.A.A. Peffer, J. Pérez-Ramírez, Pore size determination in modified micro- and mesoporous materials. Pitfalls and limitations in gas adsorption data analysis, Microporous Mesoporous Mater. 60 (2003) 1-17.
[27] F. Fantozzi, A. Frassoldati, P. Bartocci, G. Cinti, F. Quagliarini, G. Bidini, E.M. Ranzi, An experimental and kinetic modeling study of glycerol pyrolysis, Appl. Energy 184 (2016) 68-76.
[28] E.B. Hemings, C. Cavallotti, A. Cuoci, T. Faravelli, E. Ranzi, A detailed kinetic study of pyrolysis and oxidation of glycerol (propane-1,2,3-triol), Combust. Sci. Technol. 184 (2012) 1164-1178.
[29] Y.S. Stein, M.J. Antal, M. Jones, A study of the gas-phase pyrolysis of glycerol, J. Anal. Appl. Pyrolysis 4 (1983) 283-296.
[30] H. Park, Y.S. Yun, T.Y. Kim, K.R. Lee, J. Baek, J. Yi, Kinetics of the dehydration of glycerol over acid catalysts with an investigation of deactivation mechanism by coke, Appl. Catal., B 176 (2015) 1-10.
[31] K.S.W. Sing, D.H. Everett, R.A.W. Haul, L. Moscou, R.A. Pierotti, J. Rouquerol, T. Siemieniewska, Reporting physisorption data for gas/solid systems with special reference to the determination of surface area and porosity, Pure Appl. Chem. 57 (1985) 603-619.
[32] L.-C. Wang, Y. Zhang, J. Xu, W. Diao, S. Karakalos, B. Liu, X. Song, W. Wu, T. He, D. Ding, Non-oxidative dehydrogenation of ethane to ethylene over ZSM-5 zeolite supported iron catalysts, Appl. Catal., B 256 (2019) 117816.
[33] N. Viswanadham, R. Kamble, M. Singh, M. Kumar, G. Murali Dhar, Catalytic properties of nano-sized ZSM-5 aggregates, Catal. Today 141 (2009) 182-186.
[34] D. Li, Y. Chen, J. Hu, B. Deng, X. Cheng, Y. Zhang, Synthesis of Hierarchical Chabazite Zeolite via Interzeolite Transformation of Coke-containing Spent MFI, Appl. Catal., B 270 (2020) 118881.
[35] Y. Ni, A. Sun, X. Wu, G. Hai, J. Hu, T. Li, G. Li, The preparation of nano-sized H[Zn, Al]ZSM-5 zeolite and its application in the aromatization of methanol, Microporous Mesoporous Mater. 143 (2011) 435-442.
[36] M.M.J. Treacy, J.B. Higgins, MFI - ZSM-5, Calcined, Collection of simulated xrd powder patterns for zeolites (Fifth edition), Elsevier Science B.V., Amsterdam, 2007, pp. 278-279.
[37] S. Kim, G. Park, S.K. Kim, Y.T. Kim, K.-W. Jun, G. Kwak, Gd/HZSM-5 catalyst for conversion of methanol to hydrocarbons: Effects of amounts of the Gd loading and catalyst preparation

method, Appl. Catal., B 220 (2018) 191-201.
[38] A.S. Al-Dughaither, H. de Lasa, HZSM-5 zeolites with different SiO_2/Al_2O_3 ratios. Characterization and NH_3 desorption kinetics, Ind. Eng. Chem. Res. 53 (2014) 15303-15316.
[39] E.F. Iliopoulou, E. Heracleous, A. Delimitis, A.A. Lappas, Producing high quality biofuels: Pt-based hydroisomerization catalysts evaluated using BtL-naphtha surrogates, Appl. Catal., B 145 (2014) 177-186.
[40] T.C. Hoff, R. Thilakaratne, D.W. Gardner, R.C. Brown, J.-P. Tessonnier, Thermal stability of aluminum-rich ZSM-5 zeolites and consequences on aromatization reactions, J. Phys. Chem. C 120 (2016) 20103-20113.
[41] C.S. Triantafillidis, A.G. Vlessidis, L. Nalbandian, N.P. Evmiridis, Effect of the degree and type of the dealumination method on the structural, compositional and acidic characteristics of H-ZSM-5 zeolites, Microporous Mesoporous Mater. 47 (2001) 369-388.
[42] Z.W. Yu, S.H. Li, Q. Wang, A.M. Zheng, X. Jun, L. Chen, F. Deng, Bronsted/Lewis Acid Synergy in H-ZSM-5 and H-MOR Zeolites Studied by H-1 and Al-27 DQ-MAS Solid-State NMR Spectroscopy, J. Phys. Chem. C 115 (2011) 22320-22327.
[43] K. Ramesh, C. Jie, Y.F. Han, A. Borgna, Synthesis, characterization, and catalytic activity of phosphorus modified H-ZSM-5 catalysts in selective ethanol dehydration, Ind. Eng. Chem. Res. 49 (2010) 4080-4090.
[44] M.I. Zaki, M.A. Hasan, F.A. Al-Sagheer, L. Pasupulety, In situ FTIR spectra of pyridine adsorbed on SiO_2-Al_2O_3, TiO_2, ZrO_2 and CeO_2: general considerations for the identification of acid sites on surfaces of finely divided metal oxides, Colloids Surf., A 190 (2001) 261-274.
[45] A. Martin, U. Wolf, S. Nowak, B. Lucke, Pyridine-IR investigations of hydrothermally treated dealuminated HZSM-5 zeolites, Zeolites 11 (1991) 85-92.
[46] Y. Lou, J. Ma, W.D. Hu, Q.G. Dai, L. Wang, W.C. Zhan, Y.L. Guo, X.M. Cao, Y. Guo, P. Hu, G.Z. Lu, Low-temperature methane combustion over Pd/H-ZSM-5: Active Pd sites with specific electronic properties modulated by acidic sites of H-ZSM-5, ACS Catal. 6 (2016) 8127-8139.
[47] X. Long, Q. Zhang, Z.-T. Liu, P. Qi, J. Lu, Z.-W. Liu, Magnesia modified H-ZSM-5 as an efficient acidic catalyst for steam reforming of dimethyl ether, Appl. Catal., B 134-135 (2013) 381-388.
[48] J.-P. Gilson, G.C. Edwards, A.W. Peters, K. Rajagopalan, R.F. Wormsbecher, T.G. Roberie, M.P. Shatlock, Penta-co-ordinated aluminium in zeolites and aluminosilicates, Journal of the Chemical Society, Chemical Communications (1987) 91-92.
[49] M.-C. Silaghi, C. Chizallet, J. Sauer, P. Raybaud, Dealumination mechanisms of zeolites and extra-framework aluminum confinement, J. Catal. 339 (2016) 242-255.
[50] H.C. Genuino, I. Muizebelt, A. Heeres, N.J. Schenk, J.G.M. Winkelman, H.J. Heeres, An improved catalytic pyrolysis concept for renewable aromatics from biomass involving a recycling strategy for co-produced polycyclic aromatic hydrocarbons, Green Chem. 21 (2019) 3802-3806.